

Spatial IMA1 regulation restricts root iron acquisition on MAMP perception

<https://doi.org/10.1038/s41586-023-06891-y>

Received: 14 October 2022

Accepted: 22 November 2023

Published online: 10 January 2024

 Check for updates

Min Cao¹, Matthieu Pierre Platret¹, Huei-Hsuan Tsai², Ling Zhang¹, Tatsuya Nobori^{1,3,4}, Laia Armengot^{5,6}, Yintong Chen¹, Wenrong He¹, Lukas Brent¹, Nuria S. Coll^{5,7}, Joseph R. Ecker^{1,3,4}, Niko Geldner² & Wolfgang Busch^{1,8} 

Iron is critical during host–microorganism interactions^{1–4}. Restriction of available iron by the host during infection is an important defence strategy, described as nutritional immunity⁵. However, this poses a conundrum for externally facing, absorptive tissues such as the gut epithelium or the plant root epidermis that generate environments that favour iron bioavailability. For example, plant roots acquire iron mostly from the soil and, when iron deficient, increase iron availability through mechanisms that include rhizosphere acidification and secretion of iron chelators^{6–9}. Yet, the elevated iron bioavailability would also be beneficial for the growth of bacteria that threaten plant health. Here we report that microorganism-associated molecular patterns such as flagellin lead to suppression of root iron acquisition through a localized degradation of the systemic iron-deficiency signalling peptide Iron Man 1 (IMA1) in *Arabidopsis thaliana*. This response is also elicited when bacteria enter root tissues, but not when they dwell on the outer root surface. IMA1 itself has a role in modulating immunity in root and shoot, affecting the levels of root colonization and the resistance to a bacterial foliar pathogen. Our findings reveal an adaptive molecular mechanism of nutritional immunity that affects iron bioavailability and uptake, as well as immune responses.

Iron is an essential nutrient for organismal growth throughout all branches of life^{10,11}. Although iron is among the most common elements on our planet, its bioavailability in most environments is low and is a limiting factor for growth. Consequently, strong competition for iron is common between organisms. In mammals, iron levels have a direct impact on the composition of the gut microbiota^{1,2} and can modulate host inflammatory responses restricting iron availability for pathogenic microorganisms⁵. In plants, iron-limited soil environments trigger the activation of coumarin secretion in roots, which contributes to the alteration of the root-associated microbiota^{3,4}. Conversely, the soil-borne bacterial community can also have a considerable impact on root iron acquisition^{3,12,13}. On the other side of the spectrum, pathogens can compete for and restrict iron for plants^{14,15}, plant immunity responses affect bacterial iron homeostasis¹⁶ and beneficial microorganisms can produce siderophores that pathogens cannot use, consequently suppressing pathogen growth^{17,18}. Overall, iron has an important but complex role in regulating plant–microorganism interactions. However, much about this multifaceted interaction that includes plants, beneficial or commensal and pathogenic microorganisms in the rhizosphere¹⁹ remains to be learned.

Flg22 represses root responses to –Fe

We previously found a pronounced interplay of responses to low iron and immunity within the first few hours after roots were exposed to

an iron-depletion environment²⁰. To investigate this interplay at a longer timescale, we grew *Arabidopsis* seedlings in iron-sufficient and low-iron media with and without the elicitor flg22, a peptide fragment of bacterial flagellin (Fig. 1a). Compared with seedlings grown under iron-sufficient conditions (+Fe), seedlings grown under low-iron conditions (–Fe) were slightly more chlorotic and contained less iron. This was exacerbated substantially after co-treatment with flg22 (Fig. 1a–c and Extended Data Fig. 1a), but not when treated with a non-immunogenic form of flagellin, flg20 (Extended Data Fig. 1b,c). We therefore hypothesized that flg22 abolishes root iron uptake. To test this hypothesis, we measured ferric chelate reductase (FCR) activity and expression of IRON REGULATED TRANSPORTER1 (IRT1), which are part of the canonical iron-deficiency response in *Arabidopsis* and facilitate iron uptake. Whereas FCR activity in roots was induced under –Fe without flg22 treatment, FCR activity was not induced under –Fe conditions in the presence of flg22 (Fig. 1d and Extended Data Fig. 1d). Similarly, a lack of iron triggered the induction of the *pIRT1::NLS-2xYpet* marker²⁰ in the epidermal cells of the differentiation zone, and treatment with flg22, but not flg20, abolished these responses (Fig. 1e,f and Extended Data Fig. 1e). IRT1 protein levels reflected this response (Fig. 1g and Extended Data Fig. 1f–h). This was dependent on flg22 reception by the FLS2 immune receptor as flg22-induced chlorosis, and flg22-triggered FCR activity and IRT1 repression under –Fe conditions were abolished in *fls2* mutants (Extended Data Fig. 1i–m). Overall, these data demonstrated

¹Plant Molecular and Cellular Biology Laboratory, Salk Institute for Biological Studies, La Jolla, CA, USA. ²Department of Plant Molecular Biology, University of Lausanne, Lausanne, Switzerland.

³Genomic Analysis Laboratory, Salk Institute for Biological Studies, La Jolla, CA, USA. ⁴Howard Hughes Medical Institute, Salk Institute for Biological Studies, La Jolla, CA, USA. ⁵Centre for Research in Agricultural Genomics (CRAG), CSIC-IRTA-UAB-UB, Campus UAB, Bellaterra, Spain. ⁶Department of Genetics, Microbiology and Statistics, Universitat de Barcelona, Barcelona, Spain.

⁷Consejo Superior de Investigaciones Científicas (CSIC), Barcelona, Spain. ⁸Integrative Biology Laboratory, Salk Institute for Biological Studies, La Jolla, CA, USA.  e-mail: wbusch@salk.edu

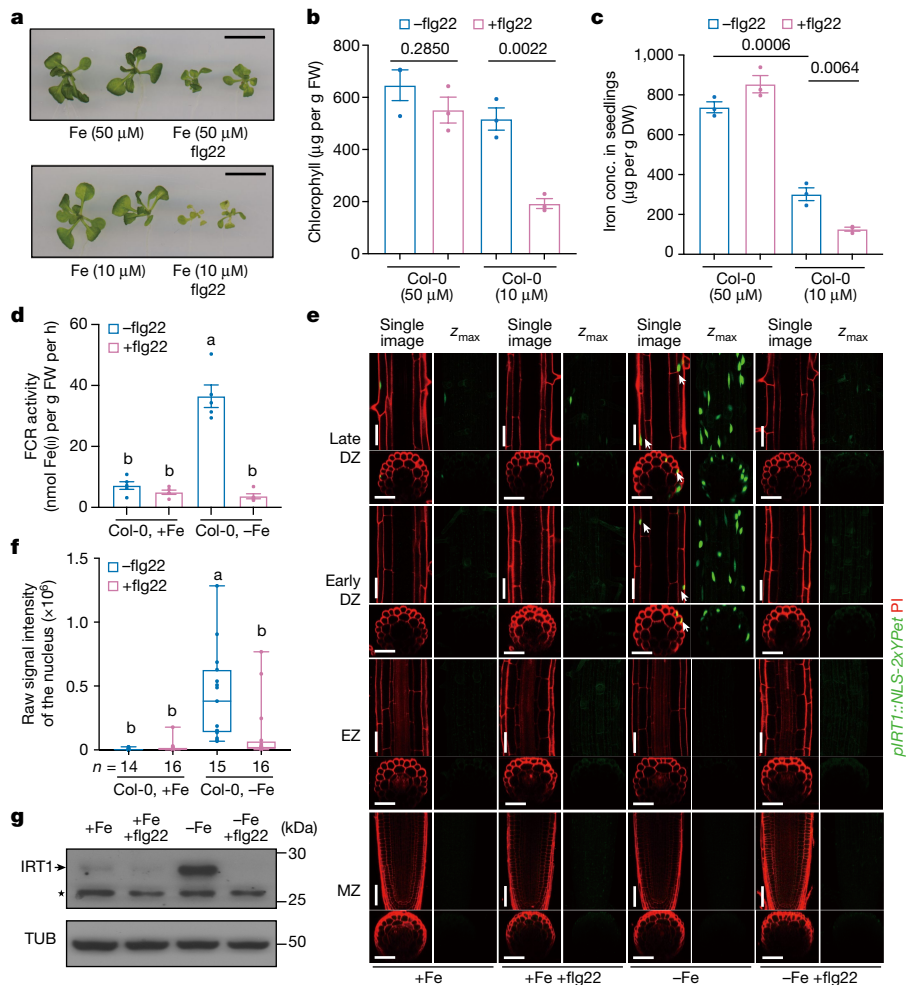


Fig. 1 | flg22 represses iron uptake during iron deficiency. **a–c**, The leaves of 15-day-old *Arabidopsis* seedlings, which were grown under iron-sufficient (50 μM) or low-iron (10 μM) conditions with or without low levels of flg22 (10 nM) treatment. **a**, The shoots. Scale bar, 1 cm. **b**, The total chlorophyll concentration of the Col-0 shoots. FW, fresh weight. **c**, The iron concentration of Col-0 seedlings. Three biological replicates. Data are mean ± s.e.m. Statistical analysis was performed using two-sided *t*-tests. DW, dry weight. **d**, FCR activity in Col-0 roots that were grown for 7 days under +Fe conditions and transferred to +Fe, +Fe +flg22, -Fe or -Fe +flg22 liquid medium for 2 days. Five biological replicates. Data are mean ± s.e.m. Different letters indicate statistically significant differences between different conditions analysed using one-way analysis of variance (ANOVA) followed by Tukey's test ($P < 0.05$). **e**, Promoter activity of *IRT1* in the roots of *pRT1::NLS-2xYpet* seedlings in response to +Fe, +Fe +flg22, -Fe and -Fe +flg22 treatment. Seedlings were grown on the +Fe

medium and, after 5 days, were transferred to the different liquid medium for 24 h treatment. DZ, differentiation zone; EZ, elongation zone; MZ, meristematic zone. Green, nuclear-localized Ypet; red, propidium iodide (PI) cell wall stain. For each treatment, a representative single confocal section (single image, GFP and PI), a maximum-intensity z-projection (z_{max} , GFP only), a single optical section of the transverse view and a z-projection of the transverse section are shown. Scale bar, 50 μm. **f**, Raw signal intensity quantification of the *pRT1* reporter. Different letters indicate statistically significant differences between different conditions analysed using one-way ANOVA followed by Tukey's test ($P < 0.05$). **g**, Western blot analysis of *IRT1* protein levels in Col-0 roots grown under +Fe, +Fe +flg22, -Fe and -Fe +flg22 conditions. The arrow indicates the *IRT1* protein band. The star indicates a non-specific band. Tubulin (TUB) protein was the internal control.

that flg22-elicited immune responses can repress the iron-deficiency program.

The notable effect of flg22-triggered repression on iron-deficiency responses prompted us to test other microorganism-associated molecular patterns (MAMPs). The bacteria-derived MAMPs flg22 and elf18 triggered immune responses in the root tip and chitin, and a fungal-derived MAMP triggered immune responses in the differentiation zone as indicated by the upregulation of the reporters for several defence genes such as *FRK1*, *MYB51* and *CYP71A12* (Extended Data Fig. 2a–c). Like flg22, elf18 also repressed FCR activity and *IRT1* activation under -Fe conditions in differentiated epidermal cells (Extended Data Fig. 2d–f). However, chitin treatment neither repressed FCR activity nor *IRT1* activation under -Fe conditions (Extended Data Fig. 2d–f). Taken together, our results suggest that different MAMPs modulate iron-deficiency responses in the root in a specific manner.

IMA1 facilitates flg22–Fe cross-talk

The induction of FCR and *IRT1* after iron deficiency is controlled by the transcription factor FIT²¹. However, flg22 was still able to strongly repress *IRT1* protein accumulation in plants that constitutively over-express FIT (Extended Data Fig. 2g), suggesting that this response to flg22 is not dependent on a regulation of FIT. To elucidate the program responsible for the flg22 triggered repression of *IRT1*, we conducted RNA-seq analysis of roots grown under +Fe and/or -Fe conditions. During the response to flg22, the expression of a large portion of iron-responsive genes was modulated (Fig. 2a). The most significantly overlapping gene sets were constituted by genes that were downregulated in response to -Fe conditions and upregulated in response to -Fe with flg22 (hypergeometric test; $P < 2.98 \times 10^{-139}$) and vice versa (hypergeometric test; $P < 2.08 \times 10^{-92}$) (Extended

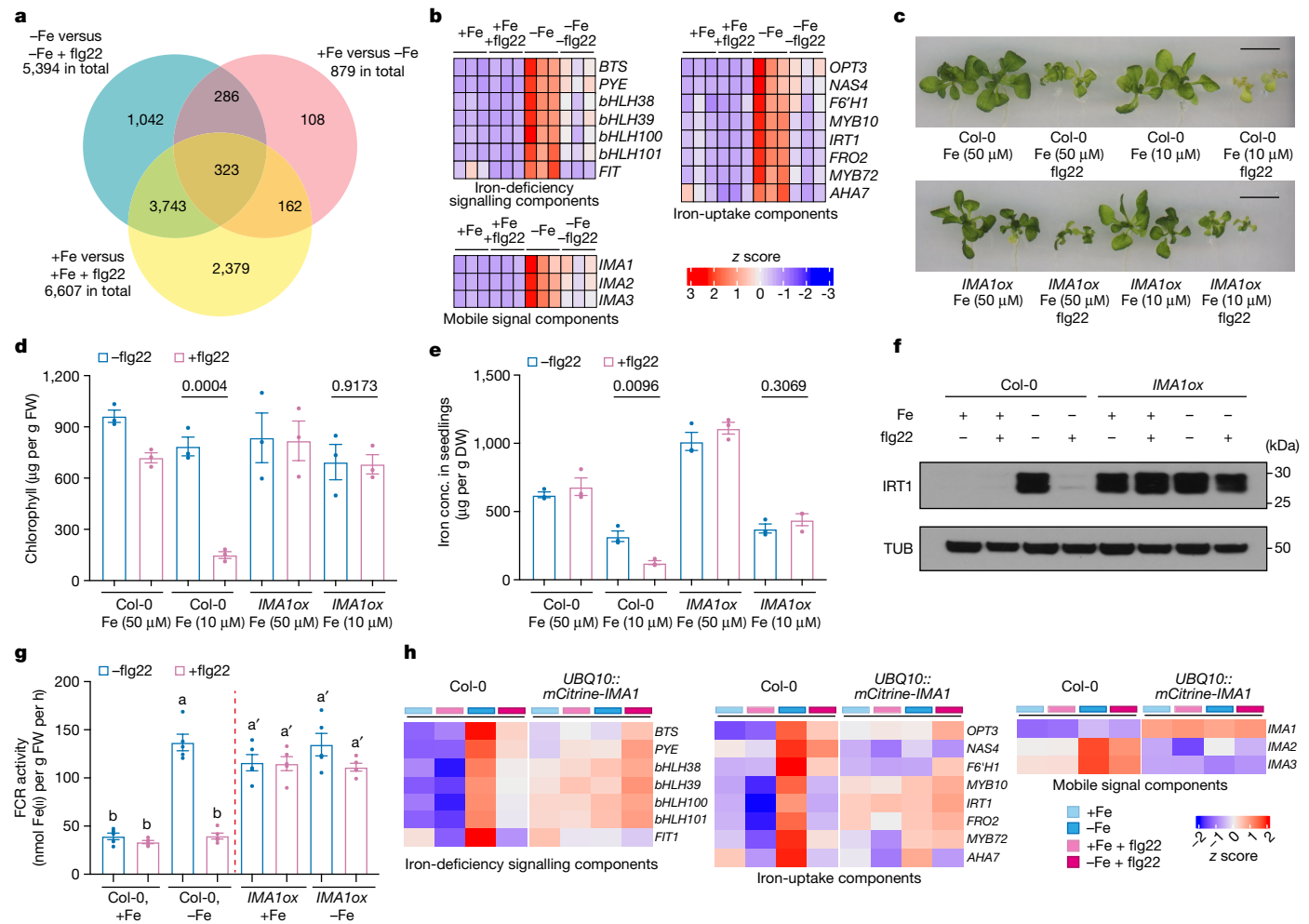


Fig. 2 | flg22 represses iron-deficiency responses through IMA1. **a**, RNA-seq analysis of DEGs. **b**, Mean-centred z scores for well-known iron-responsive genes (three independent biological repeats): iron-deficiency signalling components, iron-uptake components and long-distance signalling components. **c–e**, The phenotypes in 15-day-old Col-0 and *IMA1ox* seedlings in response to iron-sufficient (50 μM) or low-iron (10 μM) conditions with or without low levels of flg22 treatment (10 nM). **c**, The shoots. Scale bar, 1 cm. **d**, Total chlorophyll concentrations of shoots. **e**, Iron concentration of seedlings. For **d** and **e**, three biological replicates. Data are mean ± s.e.m. **f**, P values were calculated using two-tailed Student's *t*-tests. **f**, Western blot analysis of IRT1 protein levels in Col-0 and *IMA1ox* roots in response to +Fe, +Fe + flg22, -Fe and -Fe + flg22 treatment. The internal control was tubulin. **g**, Quantitative analysis of FCR activities in Col-0 and *IMA1ox* roots grown for 7 days under +Fe conditions and transferred to +Fe, +Fe + flg22, -Fe and -Fe + flg22 liquid medium for 2 days. Five biological replicates. Data are mean ± s.e.m. Different letters indicate statistically significant differences between different conditions analysed using one-way ANOVA followed by Tukey's test ($P < 0.05$). **h**, Mean-centred z scores (normalized to Col-0, +Fe) for well-known iron-responsive genes.

two-tailed Student's *t*-tests. **f**, Western blot analysis of IRT1 protein levels in Col-0 and *IMA1ox* roots in response to +Fe, +Fe + flg22, -Fe and -Fe + flg22 treatment. The internal control was tubulin. **g**, Quantitative analysis of FCR activities in Col-0 and *IMA1ox* roots grown for 7 days under +Fe conditions and transferred to +Fe, +Fe + flg22, -Fe and -Fe + flg22 liquid medium for 2 days. Five biological replicates. Data are mean ± s.e.m. Different letters indicate statistically significant differences between different conditions analysed using one-way ANOVA followed by Tukey's test ($P < 0.05$). **h**, Mean-centred z scores (normalized to Col-0, +Fe) for well-known iron-responsive genes.

Data Fig. 3a). *k*-means clustering of all differentially expressed genes (DEGs) that responded to flg22, -Fe or both (-Fe + flg22 double treatment) led to five clusters of which the genes showed distinct expression patterns (Extended Data Fig. 3b). Cluster 5 was of most interest to us as it contained genes that were induced by -Fe, but strongly repressed by additional flg22 treatment. A Gene Ontology (GO) enrichment analysis of the genes contained in cluster 5 revealed that this gene list was highly enriched for the GO term 'response to iron starvation'. Among genes in cluster 5 were many of the canonical iron-deficiency-responsive genes, including those related to iron-deficiency signalling (*BTS*, *PYE*, *bHLH38*, *bHLH39*, *bHLH100*, *bHLH101*), iron-uptake-related components (*OPT3*, *NAS4*, *F6'H1*, *MYB10*, *IRT1*, *FRO2*, *MYB72*, *AHA7*) and mobile-iron-deficiency signalling (*IMA1*, *IMA2*, *IMA3*) (Fig. 2b). As expected, these responses were not observable in *fls2* mutant plants that do not perceive flg22 (Extended Data Fig. 3c–f). The extensive and distinct interplay of gene expression changes induced by flg22 and -Fe suggested that flg22 represses iron-deficiency signalling by regulating key components of the iron-deficiency signalling pathway.

Notably, flg22 repressed the upregulation of three IMAs in the root after -Fe treatment (Fig. 2b). As IMAs act upstream of most known iron deficiency responses, including *FIT*²², we reasoned that IMAs might be downstream of the flg22 signalling relay. We therefore tested the overexpression line *IMA1ox* in which the iron-deficiency pathway is constitutively activated under our conditions. The Flg22-triggered leaf chlorosis and reduced iron concentration in the -Fe-treated seedlings were largely restored in *IMA1ox* seedlings (Fig. 2c–e). Moreover, iron-deficiency-induced IRT1 accumulation and FCR activation were insensitive to flg22 treatment under -Fe conditions in the *IMA1ox* line (Fig. 2f,g). An RNA-seq experiment using *UBQ10::mCitrine-IMA1* and wild-type (WT) plants showed that, in contrast to in Col-0, in which a large proportion of genes that were upregulated under -Fe conditions were downregulated in the -Fe + flg22 (227 out of 457, 49.7%; $P = 2.08 \times 10^{-92}$, hypergeometric test) treatment group, there was no significant overlap of such genes in *UBQ10::mCitrine-IMA1* plants (Extended Data Fig. 4a (bottom); 50 out of 457, 10.9%; $P = 0.99$, hypergeometric test). The -Fe-induced genes in Col-0 were upregulated in *UBQ10::mCitrine-IMA1* under +Fe conditions, and showed less

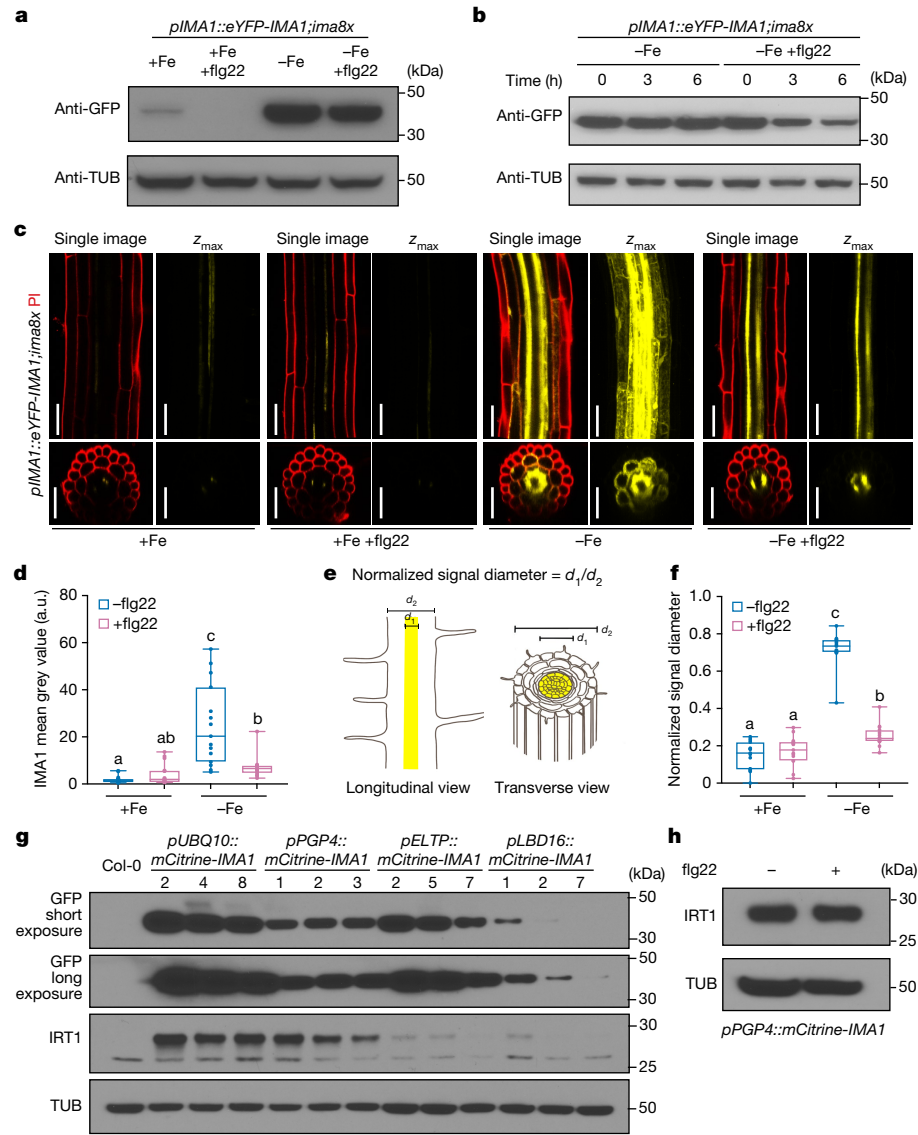


Fig. 3 | flg22 spatially represses IMA1 in the ground tissue of the root. **a, b**, IMA1 protein levels in *pIMA1::eYFP-IMA1;ima8x* roots. The internal control was tubulin. **a**, Response to the +Fe, +Fe + flg22, -Fe and -Fe + flg22 treatments. **b**, Time course: seedlings were pretreated with -Fe for 36 h, then treated with -Fe or -Fe + flg22 (1 μ M flg22) for 0, 3 and 6 h. **c**, The distribution of IMA1 in response to +Fe, +Fe + flg22, -Fe and -Fe + flg22 treatment in the differentiation zone of the root. Five-day-old *pIMA1::eYFP-IMA1;ima8x* seedlings were grown on +Fe medium and then transferred to liquid treatment medium for 24 h. Yellow, eYFP-IMA1; red, PI cell wall stain. For each treatment, a representative single confocal section (single image, eYFP/PI), a maximal z-projection of the z-stack (z_{\max} , eYFP only), a single optical section of the transverse view and a z-projection of the transverse section are shown. Scale bar, 50 μ m. **d**, Quantification of the IMA1 fluorescence signal intensity in the differentiation zone of *pIMA1::eYFP-IMA1;ima8x* roots. $n = 15$ biologically independent seedlings. Statistical analysis was performed using two-tailed Kruskal–Wallis tests followed by multiple pairwise comparisons using the two-tailed Steel–Dwass–Critchlow–Fligner procedure ($P < 0.05$). **e**, Schematic of the quantification method for the normalized signal diameter. **f**, Quantification of the normalized IMA1 signal diameter under different treatment conditions in the differentiation zones of *pIMA1::eYFP-IMA1;ima8x* roots. $n = 15$ biologically independent seedlings. Statistical analysis was performed using two-tailed Kruskal–Wallis tests followed by multiple pairwise comparisons using the two-tailed Steel–Dwass–Critchlow–Fligner procedure ($P < 0.05$). **g, h**, Western blot analysis of IRT1 protein levels in the roots of transgenic plants with different tissue-specific promoters driving *IMA1* expression. The internal control was tubulin. **g**, All seedlings were grown in +Fe to avoid endogenous induction of IRT1 by low iron. Three independent lines of each transgenic plant are shown (Extended Data Fig. 6e). **h**, *pPGP4::mCitrine-IMA1* roots in response to treatment with +Fe and +Fe + flg22.

followed by multiple pairwise comparisons using the two-tailed Steel–Dwass–Critchlow–Fligner procedure ($P < 0.05$). **e**, Schematic of the quantification method for the normalized signal diameter. **f**, Quantification of the normalized IMA1 signal diameter under different treatment conditions in the differentiation zones of *pIMA1::eYFP-IMA1;ima8x* roots. $n = 15$ biologically independent seedlings. Statistical analysis was performed using two-tailed Kruskal–Wallis tests followed by multiple pairwise comparisons using the two-tailed Steel–Dwass–Critchlow–Fligner procedure ($P < 0.05$). **g, h**, Western blot analysis of IRT1 protein levels in the roots of transgenic plants with different tissue-specific promoters driving *IMA1* expression. The internal control was tubulin. **g**, All seedlings were grown in +Fe to avoid endogenous induction of IRT1 by low iron. Three independent lines of each transgenic plant are shown (Extended Data Fig. 6e). **h**, *pPGP4::mCitrine-IMA1* roots in response to treatment with +Fe and +Fe + flg22.

sensitivity to flg22 treatment (Extended Data Fig. 4b–d). Consistent with previous findings²³, expression levels of IMA2 and IMA3 were decreased in *UBQ10::mCitrine-IMA1* plants compared with in Col-0 plants throughout all of the treatment conditions, suggesting that there might be a gene dosage compensation mechanism within the IMA gene family (Fig. 2h). We also examined the expression levels of key flg22-dependent pattern-triggered immunity (PTI) components^{24,25} and found that some of these were also affected by IMA1 overexpression (Extended Data Fig. 4e). Taken together, our data show that the

repression of iron deficiency responses by flg22 is abolished when IMA1 is continuously expressed, that the flg22 modulation of iron-deficiency responses involve a downregulation of IMAs and that IMA1 signalling can perturb expression of PTI-response genes.

flg22 causes IMA1 depletion

IMA1 is a phloem mobile signal that is triggered in response to iron deficiency²². To investigate whether and how flg22 abolishes IMA

function, we obtained the IMA octuple mutant *ima8x* and the rescue line *pIMA1::eYFP-IMA;ima8x²*. As expected, we observed that IRT1 was not induced under iron-deficiency conditions in the *ima8x* mutant line and that the *IMA1* transgene successfully rescued IRT1 induction in *ima8x* plants (Extended Data Fig. 5a). As in the WT, flg22 was able to repress IRT1 accumulation and FCR induction in *pIMA1::eYFP-IMA;ima8x* plants (Extended Data Fig. 5a,b). Notably, the highly increased eYFP-IMA1 protein levels that we observed after –Fe treatment in whole-root tissue were only slightly reduced after flg22 treatment (Fig. 3a). To investigate this partial depletion of IMA1 protein in higher detail, we pretreated *pIMA1::eYFP-IMA;ima8x* plants with –Fe to strongly elevate IMA1 protein levels, and only subsequently treated with flg22. Consistent with the previous experiment, flg22 treatment for 6 h only partially depleted the –Fe-treatment-induced IMA1 in the root (Fig. 3b). As iron-deficiency responses can be highly localized, we conducted confocal microscopy analysis of eYFP-IMA1 in the early-differentiation zone of the root, which is the region of *IRT1* induction under iron-deficient conditions^{26,27}. As expected, –Fe conditions highly induced IMA1 protein in stele, as well as in the pericycle, endodermis and cortex tissues in the roots of these seedlings (Fig. 3c,d). Concomitant treatment with –Fe and flg22 strongly reduced IMA1 protein accumulation in the endodermis and cortex and partially in the pericycle, but it did not strongly reduce IMA1 levels in the vasculature (Fig. 3c,d). To quantify this pattern, we measured the IMA1 signal diameter, and the IMA1 signal intensity profile compared with the width of the whole root (Fig. 3e and Extended Data Fig. 5h). Under –Fe conditions, the IMA1 signal spread throughout the whole width of the root. Under +Fe conditions or when treated with flg22 under –Fe conditions, the IMA1 signal was restricted around the vasculature (Fig. 3f and Extended Data Fig. 5h). As expected, these responses were abolished in the *fsl2* receptor mutant that does not perceive flg22 (Extended Data Fig. 5c–h). We next set out to understand the mechanism for this cell-type-specific depletion of IMA1 after flg22 treatment. To study a potential transcriptional regulation, we obtained *pIMA1::mCitrine-NLS-mCitrine* plants. *IMA1* transcriptional activity was low under +Fe conditions, and –Fe strongly induced *IMA1* transcription in all cell layers (Extended Data Fig. 6a,b). Notably, flg22 led to a further induction of *IMA1* transcriptional activity in the ground tissue under –Fe (Extended Data Fig. 6a,c). This suggested that the depletion of IMA1 in the ground tissue was more likely to be regulated at the post-transcriptional level.

IMA1 was previously shown to be a mobile signal²², and intercellular molecular movement can be regulated in plants by flg22-dependent callose deposition at plasmodesmata²⁸. To test whether this could explain the flg22-mediated repression of –Fe responses, we used 2-deoxy-D-glucose, a well-characterized callose synthase inhibitor²⁹. To assess this, we used *IRT1* expression as a read-out, as the repression of IMA1 in the ground tissue coincided with the flg22-elicited repression of IRT1 and FCR. We could not observe a rescue of the IRT1 protein level (Extended Data Fig. 6d). This suggested that flg22-mediated callose deposition may not have a role in regulating the iron-deficiency responses.

We next ectopically expressed mCitrine-IMA1 in a cell-type-specific manner (Extended Data Fig. 6e) and measured IRT1 induction under iron-sufficient conditions, as this enabled us to exclude the effect of endogenous IMA, which is induced only by iron deficiency. IRT1 was strongly induced in *pUBQ10::mCitrine-IMA1* (expressing in all cell layers) and *pPGP4::mCitrine-IMA1* (preferentially expressing in the epidermis and partially in the cortex) lines (Fig. 3g). This suggested that the presence of IMA1 in the epidermis/cortex is required and sufficient to induce IRT1 in the root. IRT1 was not strongly induced in the *pLBD16::mCitrine-IMA1* (pericycle) or *pELTP::mCitrine-IMA1* (endodermis) lines compared with in Col-0 WT plants (Fig. 3g). In contrast to *pIMA1::eYFP-IMA1;ima8x*, the signal of *pELTP::mCitrine-IMA1* did not extend to the outer cell layers under both +Fe and –Fe conditions,

suggesting that IMA1 needs to be locally expressed in the cortex and epidermis to induce IRT1 (Extended Data Fig. 7a–c).

We next tested whether constitutive presence of IMA1 in the epidermis and cortex was sufficient to abolish the repression of iron-deficiency responses by flg22. *pPGP4::mCitrine-IMA1* roots driving IMA1 continuously in the epidermis and cortex root tissues were insensitive to flg22-mediated IRT1 repression under +Fe conditions (Fig. 3h). However, we noted that the IMA1 levels were slightly decreased after flg22 treatment under –Fe conditions in the *pPGP4::mCitrine-IMA1* lines, suggesting that IMA1 protein was degraded in this condition (Extended Data Fig. 7d). Taken together, our data strongly suggest that flg22 treatment leads to the repression of *IRT1* and FCR activation under iron deficiency through downregulation of IMA1 in the outer tissue layers (ground tissue).

BTSLs deplete IMA1 in the ground tissue

We next investigated whether the partial degradation of IMA1 that we had observed under the –Fe with flg22 conditions acted through the ubiquitin-dependent protein-degradation pathway. MG132, an inhibitor of the 26S proteasome, strongly reduced the protein degradation of IMA1 under –Fe conditions (Extended Data Fig. 8a). As a previous study had shown that BRUTUS (BTS), a regulator of iron homeostasis, ubiquitinates IMA1 to mediate IMA1 degradation to regulate iron homeostasis³⁰, we hypothesized that BTS is required to mediate flg22-triggered IMA1 degradation. However, even though *bts-1* roots showed induced IRT1 expression and FCR activity compared with in Col-0 plants under +Fe and –Fe conditions, IRT1 expression and FCR activity, as well as IMA1 in the ground tissue were still repressed after flg22 treatment in *bts-1* mutant plants (Extended Data Fig. 8b–d). This suggested that BTS is not required for flg22-mediated IMA1 degradation and iron-deficiency-response repression. There are two *BTS* homologues in *Arabidopsis* (*BTSL1* and *BTSL2*) that are expressed in the root and function redundantly to regulate iron homeostasis³¹. To test whether BTSL1 and BTSL2 are involved in regulating flg22-mediated iron responses, we phenotyped the *btSL1,2* double mutant in response to –Fe and flg22. Compared with Col-0 plants, the *btSL1,2* mutant plants developed less leaf chlorosis in response to flg22 under low-iron conditions, suggesting that *btSL1,2* plants are less sensitive to the flg22-triggered repression of iron-deficiency responses (Fig. 4a–c). Consistent with the chlorosis phenotype, FCR activity and IRT1 protein accumulation were significantly less responsive to flg22 treatment under –Fe conditions in *btSL1,2* mutant plants compared with in Col-0 plants (Fig. 4d,e). These data suggest that *BTSL1* and *BTSL2* are required for regulating flg22-mediated repression of iron-deficiency responses.

Next, we analysed the expression pattern of *BTSL1* and *BTSL2* using plants carrying *pBTSL1-GFP* and *pBTSL2-GFP* transcriptional reporters³¹. We observed that the expression levels of *BTSL1* and *BTSL2* were induced under –Fe conditions (Fig. 4f). *BTSL1* is mainly expressed in the epidermis in response to iron deficiency. flg22 strongly repressed *BTSL1* expression under –Fe conditions. This was in contrast to *BTSL2*, which is expressed in the entire ground tissue under iron-deficiency conditions. Treatment with flg22 did not repress *BTSL2* expression (Fig. 4f). As the spatial expression patterns of *BTSL1* and *BTSL2* coincided with the area in which IMA1 was repressed after flg22 treatment, we hypothesized that *BTSL1* and *BTSL2* are involved in flg22-regulated IMA1 depletion in the ground tissue. IMA1 protein levels were reduced after flg22 treatment in *pIMA1::eYFP-IMA1;ima8x* plants but not in *pIMA1::eYFP-IMA1;btSL1,2* plants (Extended Data Fig. 8e,f). Consistent with our hypothesis, the strong increase in IMA1 in the ground tissue after iron deficiency was not abolished by flg22 treatment in *btSL1,2* plants (Fig. 4g–i and Extended Data Fig. 8g). Cycloheximide treatment decreased IMA1 levels under –Fe conditions, particularly in the epidermis and cortex, similarly to the effect of flg22, indicating that IMA1 is degraded under low-iron conditions. This reduction of IMA1 by either cycloheximide or flg22

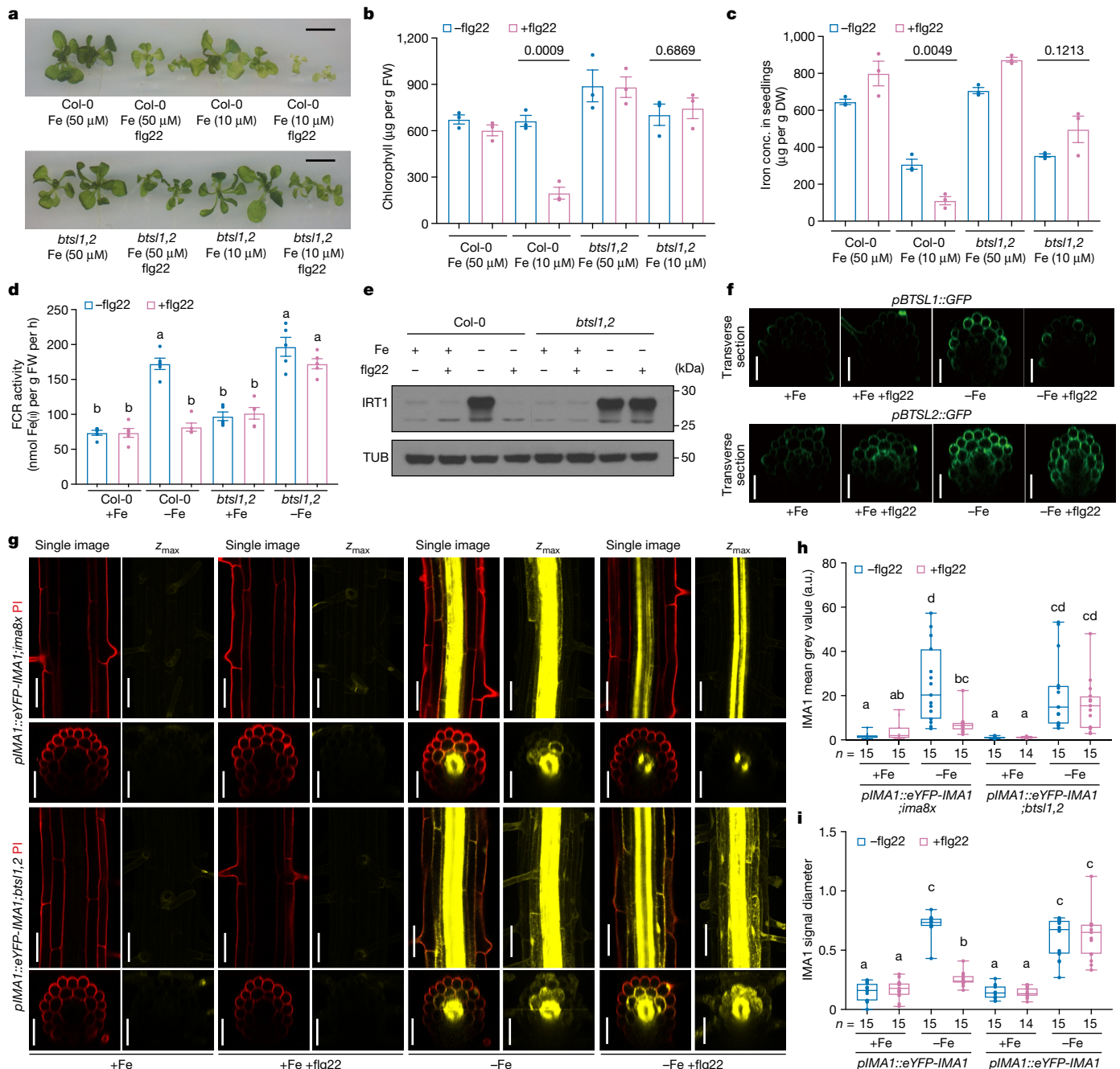


Fig. 4 | flg22 represses iron-deficiency responses by IMA1 degradation through BTSL1 and BTSL2. **a–c**, 15-day-old seedlings in +Fe (50 μ M) or –Fe (10 μ M) without or with low levels of flg22 (10 nM) treatment. **a**, The shoots. Scale bar, 1 cm. **b**, The total chlorophyll concentrations of the shoots. **c**, The iron concentration of seedlings. For **b** and **c**, three biological replicates. Data are mean \pm s.e.m. P values were calculated using two-tailed Student's t-tests. **d**, FCR activities in Col-0 and btsl1,2 roots grown for 7 days under +Fe and transferred to +Fe, +Fe + flg22, –Fe and –Fe + flg22 liquid medium for 2 days. Five biological replicates. Data are mean \pm s.e.m. Statistical analysis was performed using one-way ANOVA followed by Tukey's test ($P < 0.05$). **e**, Western blot analysis of IRT1 protein levels in Col-0 and btsl1,2 roots in the +Fe, +Fe + flg22, –Fe and –Fe + flg22 treatment groups. The control was tubulin. **f**, Transverse confocal microscopy sections of root differentiation zones of pBTSL1-GFP and pBTSL2-GFP in response to +Fe, +Fe + flg22, –Fe and –Fe + flg22 treatments. Green, GFP channel. Scale bar, 50 μ m. **g**, Confocal microscopy images of IMA1

in the root differentiation zone for the +Fe, +Fe + flg22, –Fe and –Fe + flg22 treatment groups. *pIMA1::eYFP-IMA1;ima8x* and *pIMA1::eYFP-IMA1;btSL1,2* seedlings (aged 5 days) were grown on +Fe medium, then transferred to liquid treatment medium for 24 h. Yellow, eYFP-IMA1; red, PI cell wall stain. Shown per treatment are a representative single confocal section (single image, eYFP and PI), a maximal z-projection (z_{\max} , eYFP only), a single optical section of the transverse view and a z-projection of the transverse section. Scale bar, 50 μ m. **h,i**, The IMA1 fluorescence signal intensity (**h**) and the normalized IMA1 signal diameter (**i**) in the root differentiation zone of *pIMA1::eYFP-IMA1;ima8x* and *pIMA1::eYFP-IMA1;btSL1,2* plants in the +Fe, +Fe + flg22, –Fe and –Fe + flg22 treatment groups. The same dataset was used as for in Fig. 3e,f for *pIMA1::eYFP-IMA1;ima8x* as the images were taken at the same time. Statistical analysis was performed using two-tailed Kruskal–Wallis tests followed by the two-tailed Steel–Dwass–Critchlow–Fligner procedure ($P < 0.05$).

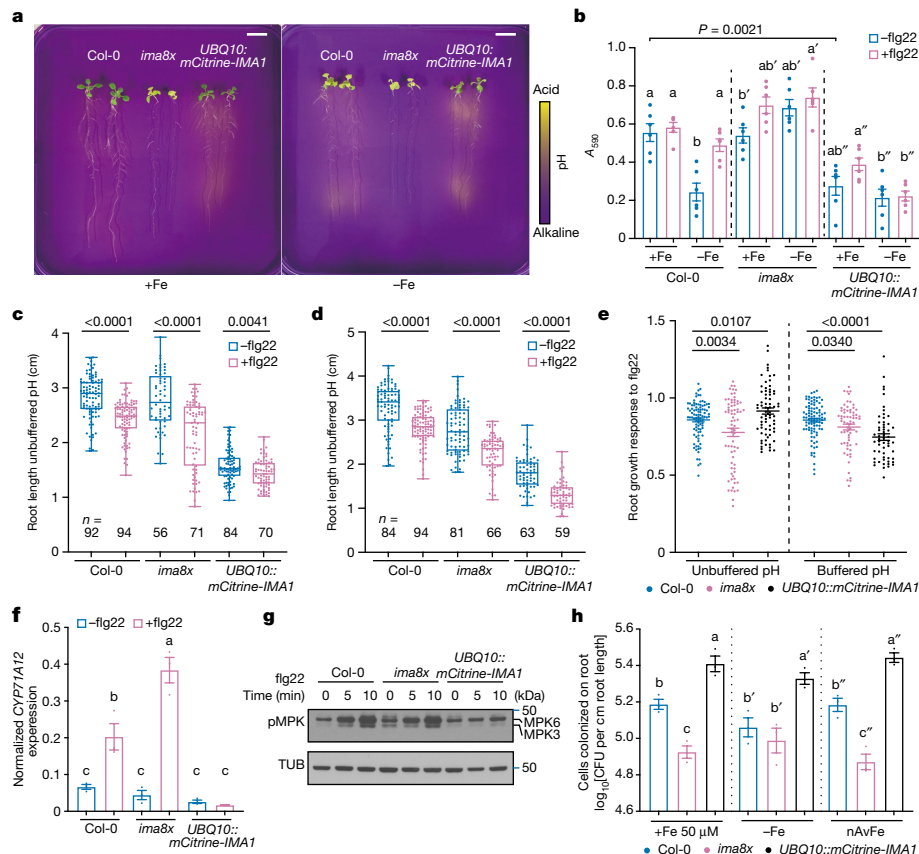


Fig. 5 | IMA1-dependent rhizosphere acidification regulates root immune responses and bacterial colonization. **a,b,** Imaging (**a**) and quantification (**b**) of rhizosphere acidification responses of Col-0, *ima8x* and *UBQ10::mCitrine-IMA1* plants after +Fe and -Fe treatment. Bromocresol purple was used as the pH indicator. **b**, Standard medium acidification by Col-0, *ima8x* and *UBQ10::mCitrine-IMA1* plants in response to treatment with +Fe, +Fe + flg22, -Fe and -Fe + flg22. Six biological replicates. Data are mean \pm s.e.m. Statistical analysis (within each genotype) was performed using one-way ANOVA followed by Tukey's test ($P < 0.05$). Two-tailed Student's *t*-tests were used to show statistically significant differences in medium acidification between Col-0 and *UBQ10::mCitrine-IMA1* plants under +Fe conditions. **c,d**, Quantification of the root length of Col-0, *ima8x* and *UBQ10::mCitrine-IMA1* plants under +Fe and +Fe + flg22 conditions without MES-KOH (**c**) and with 1 mM MES-KOH (**d**). *P* values were calculated using two-tailed Student's *t*-tests. **e**, Quantification of flg22-mediated root growth responses (+flg22/-flg22, root length of +flg22 divided

by mean of -flg22) of Col-0, *ima8x* and *UBQ10::mCitrine-IMA1* plants with or without MES-KOH. Data are mean \pm s.e.m. *P* values were calculated using two-tailed Student's *t*-tests. **f**, *CYP71A12* transcript levels in the +Fe and +Fe + flg22 groups were analysed using qPCR with reverse transcription (RT-qPCR). Roots were treated with 1 μ M flg22 for 1 h. Expression values were normalized to *ACT2*. Three biological replicates. Data are mean \pm s.e.m. Statistical analysis was performed using one-way ANOVA followed by Tukey's test ($P < 0.05$). **g**, Western blot analysis of MAPK phosphorylation by flg22 in Col-0, *ima8x* and *UBQ10::mCitrine-IMA1* roots in response to flg22. The roots were treated with 1 μ M flg22 for 0, 5 and 10 min. The internal control was tubulin. **h**, Colonization of 7-day-old *Arabidopsis* roots at 1 day after inoculation by CHA0 under +Fe, -Fe and non-available iron (nAvFe) conditions. Three biological replicates. Data are mean \pm s.e.m. Statistical analysis was performed using one-way ANOVA followed by Tukey's test ($P < 0.05$).

was restored in *bts1,2* plants (Extended Data Fig. 8h–j), indicating that BTSL1 and BTSL2 are required for degrading IMA1 protein under these conditions.

Taken together, our data indicate that the flg22-induced suppression of the iron-deficiency response is mediated predominantly through BTSL1/2-dependent IMA1 degradation in the ground tissue of the root in the differentiation zone (Extended Data Fig. 8k).

IMA1 has root and shoot immune functions

The iron-deficiency response and an effective immune response trigger antagonistic responses in the root. For example, the iron-deficiency response includes the acidification of the rhizosphere for promoting iron solubility⁹. However, the defence response leads to an alkalization of the root meristem, which further promotes immunity³². Our data suggested that IMA1 might be a central player at the interface of both pathways. Although the role of IMA1 in iron-deficiency signalling has been well characterized, a role of IMA1 in the regulation of

immunity is lacking. We therefore first investigated whether IMA1 has a role in regulating the rhizosphere acidification capacity. We found that, under +Fe conditions, Col-0 and *ima8x* plants exhibited no acidified roots, whereas *UBQ10::mCitrine-IMA1* plants displayed constitutive root acidification (Fig. 5a,b). Iron deficiency triggered root acidification around the root tip in Col-0 plants, but not in *ima8x* plants. flg22 treatment repressed root acidification in Col-0 plants, but not in *UBQ10::mCitrine-IMA1* plants (Fig. 5a,b). This suggested that IMA depletion is required for abolishing the root acidification that is triggered by flg22.

Although *UBQ10::mCitrine-IMA1* plants showed slightly shorter roots when they were grown on iron-sufficient medium compared with Col-0 and *ima8x* plants, they exhibited less sensitivity to flg22-mediated root growth inhibition, whereas *ima8x* plants exhibited enhanced flg22-mediated root growth inhibition (Fig. 5c,e). Consistent with the data that the activity of the flg22 receptor FLS2 is dependent on environmental conditions, such as root apoplastic pH³³, the less-sensitive response of *UBQ10::mCitrine-IMA1* plants to flg22 was restored by

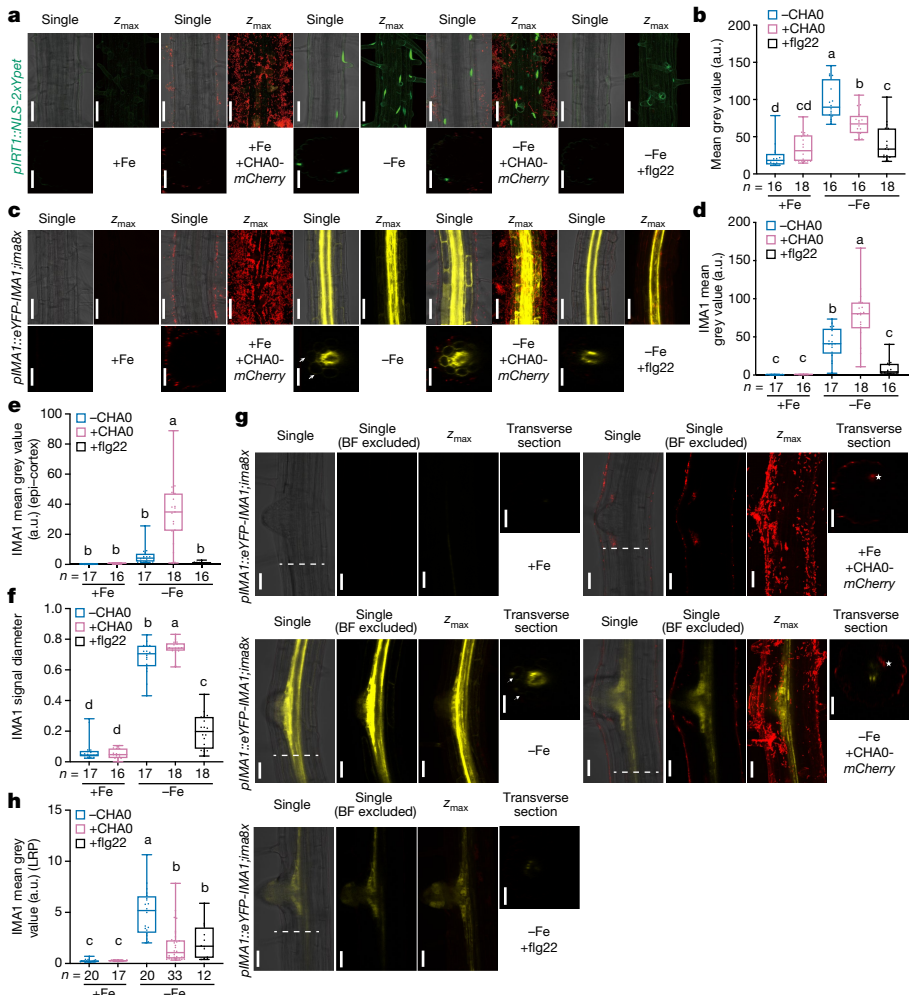


Fig. 6 | IMA1 accumulation is distinctly modulated by surface-dwelling or invading bacteria. **a**, *pIRTL::NLS-2xYpet* roots in the +Fe, +Fe + CHAO, -Fe, -Fe + CHAO and -Fe + flg22 treatment groups. Red, cell-surface-localized CHAO-*mCherry* bacteria; green, nuclear-localized Ypet. A representative single confocal section (single image, GFP and mCherry), a maximal z-projection of the z-stack (z_{\max} , GFP only) and a single optical section of the transverse view are shown. Scale bar, 50 μ m. **b**, Normalized signal quantification in *pIRTL::NLS-2xYpet* roots in the +Fe, +Fe + CHAO, -Fe, -Fe + CHAO and -Fe + flg22 treatment groups. Statistical analysis was performed using one-way ANOVA and Fisher's least significant difference (LSD) test (two-sided, $P < 0.05$). **c**, The distribution of IMA1 in the +Fe, +Fe + CHAO, -Fe, -Fe + CHAO and -Fe + flg22 treatment groups in the root differentiation zone of *pIMA1::eYFP-IMA1;ima8x* plants. Red, root surface-localized CHAO-*mCherry* bacteria; yellow, eYFP-IMA1 (yellow channel). A representative single confocal section (single image, eYFP and mCherry), a maximal z-projection of the z-stack (z_{\max} , eYFP only) and a single optical section of the transverse view are shown. Scale bar, 50 μ m. **d**, The normalized IMA1 signal intensity in the +Fe, +Fe + CHAO, -Fe, -Fe + CHAO and -Fe + flg22 treatment groups. Statistical analysis was performed using one-way ANOVA and Fisher's LSD test (two-sided, $P < 0.05$). **e**, The normalized IMA1 signal intensity in epidermis–cortex (epi–cortex) cell layers in the +Fe, +Fe + CHAO, -Fe, -Fe + CHAO and -Fe + flg22 treatment groups. Statistical analysis was performed using one-way ANOVA and Fisher's LSD test (two-sided, $P < 0.05$). **f**, The normalized IMA1 signal diameter quantification in the +Fe, +Fe + CHAO, -Fe, -Fe + CHAO and -Fe + flg22 treatment groups. Statistical analysis was performed using one-way ANOVA and Fisher's LSD test (two-sided, $P < 0.05$). **g**, Representative images of eYFP-IMA1 in the +Fe, +Fe + CHAO, -Fe, -Fe + CHAO treatment groups at emerging lateral root primordia. Red, interior-localized CHAO-*mCherry* bacteria; yellow, eYFP-IMA1 signals. The stars indicate CHAO-*mCherry* that entered the roots through the lateral root primordia site. The arrows indicate weak IMA1 signals in the cortex. Scale bar, 50 μ m. A single confocal section (single image, eYFP and mCherry), a maximal z-projection of the z-stack (z_{\max} , eYFP only) and a single optical section of the transverse view are shown. BF, bright field. Scale bar, 50 μ m. **h**, Quantification of the normalized IMA1 signal intensity in the +Fe, +Fe + CHAO, -Fe, -Fe + CHAO and -Fe + flg22 treatment groups in the lateral root primordia region. Statistical analysis was performed using one-way ANOVA and Fisher's LSD test (two-sided, $P < 0.05$).

ANOVA and Fisher's LSD test (two-sided, $P < 0.05$). **e**, The normalized IMA1 signal intensity in epidermis–cortex (epi–cortex) cell layers in the +Fe, +Fe + CHAO, -Fe, -Fe + CHAO and -Fe + flg22 treatment groups. Statistical analysis was performed using one-way ANOVA and Fisher's LSD test (two-sided, $P < 0.05$). **f**, The normalized IMA1 signal diameter quantification in the +Fe, +Fe + CHAO, -Fe, -Fe + CHAO and -Fe + flg22 treatment groups. Statistical analysis was performed using one-way ANOVA and Fisher's LSD test (two-sided, $P < 0.05$). **g**, Representative images of eYFP-IMA1 in the +Fe, +Fe + CHAO, -Fe, -Fe + CHAO treatment groups at emerging lateral root primordia. Red, interior-localized CHAO-*mCherry* bacteria; yellow, eYFP-IMA1 signals. The stars indicate CHAO-*mCherry* that entered the roots through the lateral root primordia site. The arrows indicate weak IMA1 signals in the cortex. Scale bar, 50 μ m. A single confocal section (single image, eYFP and mCherry), a maximal z-projection of the z-stack (z_{\max} , eYFP only) and a single optical section of the transverse view are shown. BF, bright field. Scale bar, 50 μ m. **h**, Quantification of the normalized IMA1 signal intensity in the +Fe, +Fe + CHAO, -Fe, -Fe + CHAO and -Fe + flg22 treatment groups in the lateral root primordia region. Statistical analysis was performed using one-way ANOVA and Fisher's LSD test (two-sided, $P < 0.05$).

adding the pH-buffering reagent MES (Fig. 5d,e). We then examined the expression of *CYP71A12*, which is a flg22-response gene of which the promoter activation has been shown to be decreased by low pH³³. *CYP71A12* induction by flg22 was impaired in *UBQ10::mCitrine-IMA1* plants, but was stronger in *ima8x* compared with in Col-0 plants (Fig. 5f). Consistent with this, the roots of *UBQ10::mCitrine-IMA1* plants showed less MAPK phosphorylation after flg22 treatment compared with the roots of Col-0 plants under iron-sufficient conditions (Fig. 5g). Overall, our data suggest that IMA1 and its effect on rhizosphere acidification is important for root responses to flg22. Iron availability has been shown to mediate root colonization by rhizobacterium *Bacillus velezensis* SQR9³⁴. As our

data suggested that IMA1 might be a central player in mediating iron and immune responses, we tested whether IMA1 has a role in mediating host–microorganism interactions. The rhizobacterium *Pseudomonas protegens* CHAO (a model commensal *P. protegens* strain that produces flagellin) showed less colonization on the roots of *ima8x* plants, whereas it colonized the roots of the *UBQ10::mCitrine-IMA1* line to a higher extent (Fig. 5h). Taken together, this suggests that IMA1 functions at the nexus of iron deficiency and root–microorganism interactions and that higher levels of IMA can facilitate elevated bacterial growth on roots.

As IMA1 is considered to be a mobile signal that relays information from the shoot to the root²², we checked whether IMA1 also has a role

Article

in coordinating iron and immune responses in the shoot. IMA1 protein levels were low in the shoot under +Fe conditions. -Fe conditions led to an accumulation of IMA1 protein in the shoot in epidermal cells, mesophyll cells and abundantly in the vascular tissue (Extended Data Fig. 9a). Treatment with flg22 under -Fe conditions decreased IMA1 protein in the epidermal cells and mesophyll cells but not in the vascular tissue (Extended Data Fig. 9a), suggesting that, like in the root, there are also cell-type-specific regulatory mechanisms for IMA1 in the shoot. By analysing *IMA1ox*-dependent transcriptome changes in the shoot from a published dataset²², we found that, besides iron-responsive genes, immune-response and systemic acquired resistance genes were enriched among the upregulated genes (Extended Data Fig. 9b). This suggests that IMA1 may also have a role in regulating immune programs in the shoot. However, we did not observe any strong differences in flg22-elicited MAPK phosphorylation in the shoot when comparing *UBQ10::mCitrine-IMA1* and Col-0 WT plants (Extended Data Fig. 9c), suggesting that the perception of flg22 or PTI signalling activation is not affected in *UBQ10::mCitrine-IMA1* plants in the shoot. To further explore this, we measured several PTI markers in the shoot tissue using quantitative PCR (qPCR) after plants had been exposed to flg22 for a short time (1 h). Immunity marker genes were slightly upregulated without flg22, and the activation was more robust with flg22 in *UBQ10::mCitrine-IMA1* compared with Col-0 plants. Moreover, ethylene and jasmonic acid biosynthesis and signalling pathways were not hyperactive in *UBQ10::mCitrine-IMA1* plants. While the observed effects in the shoot were moderate and more thorough investigations are needed, one explanation for this might be that overexpression of IMA1 in the shoot induces a subset of systemic defence responses that is different from the root. Based on this idea, we next speculated that, if the systemic defence responses were indeed induced in the shoot of the *IMA1* overexpressor, these plants might then be more resistant to foliar pathogen attacks. Consistent with this idea, *UBQ10::mCitrine-IMA1* plants were more resistant to foliar bacterial pathogen *Pseudomonas syringae* pv. tomato DC3000 (Extended Data Fig. 9e). Taken together, IMA1 has an important role in coordinating iron deficiency and immunity, but the mechanism of action in the roots and shoots may be different and might depend on the type of microorganism.

Iron, root surface and invading bacteria

Bacterial populations can positively or negatively impact plant fitness through interactions that relate to iron. For example, commensal bacterial strains can aid roots with iron acquisition^{3,35}, whereas pathogens are thought to be in competition for available iron¹⁷. Recently, a spatially defined gating mechanism for cell-damage-dependent immune receptor activation that contributed to the distinction of commensal/beneficial and pathogenic bacteria was identified³⁶. Our data had shown that iron uptake and defence programs are connected by an IMA-related mechanism in a spatially restricted manner. We therefore wanted to test whether the repression of the iron signalling by a bacterial MAMP is dependent on the location of the bacteria. For this, we inoculated roots with CHAO-*mCherry/gfp2* under -Fe conditions. In contrast to the flg22 treatment, the *pIRT1* reporter as well as the IRT1 protein induction were not fully repressed by CHAO colonization (Fig. 6a,b and Extended Data Fig. 10a), showing that root colonization by this strain of commensal bacteria does not strongly repress iron-deficiency responses. Moreover, CHAO colonization did not repress but, instead, enhanced IMA1 protein induction by -Fe, whereas flg22 partially repressed IMA1 protein induction (Fig. 6c,d and Extended Data Fig. 10b). When CHAO was colonizing solely the surface of the root, IMA1 remained present in the outer cell layer, whereas flg22 treatment confined IMA1 into the stele (Fig. 6e,f). This indicates that this commensal/beneficial bacterial strain colonization on the root surface does not necessarily repress iron-deficiency responses and that the plant is still able to take up iron.

During our inoculations, we noticed that, in some cases, CHAO (which is considered to be a non-pathogenic bacterial strain) entered the roots at lateral root primordia, a region where cracks can naturally occur³⁶. Consistent with previous findings³⁶, higher immune responses were detected when CHAO colonized at lateral root primordia (LRP) compared with growth on the surface of differentiation zone (Extended Data Fig. 10c,d). When looking at such cases systematically, we found that, when CHAO entered the primary root through the LRP, IMA1 accumulation in the primary root was strongly reduced (Fig. 6g,h). Together, our data suggest that locally gated MAMP responsiveness can lead to spatially confined IMA1 repression and thereby might contribute to allowing roots to locally shut off iron-deficiency responses when internally colonized or to continue with iron acquisition in the presence of non-invasive, surface-dwelling bacteria (Extended Data Fig. 10e).

Discussion

Our results reveal that the extended presence of the flg22 MAMP can abolish major components of the iron-deficiency response in *A. thaliana*. This seems puzzling, as transporting bioavailable iron into the root and therefore sequestering it could deplete a potential pathogen of iron. However, these responses are mounted only when bioavailable iron is scarce in the environment (otherwise the plant would not be iron deficient), therefore continuing to make iron bioavailable by exuding iron-binding compounds and protons might benefit pathogens too. Taken together, we propose that the antagonistic function between the IMA1-mediated iron deficiency response and the flg22-elicited defence response might be critical to avoid making iron bioavailable for potential pathogens and to avoid impairing plant defence responses. Our findings also indicate that the modulation of iron-deficiency responses is not a constitutive response that is triggered merely by the presence of bacteria but one that is triggered according to the presence of cues indicative of threats (for example, sustained presence of high levels of flg22 or tissue damage). This finely tuned modulation would appear to be important to maintain a healthy rhizosphere during iron-limiting conditions, as acidic (reducing) conditions and coumarins generally promote iron solubility in the rhizosphere. Shutting iron acquisition down might constitute a way to avoid enabling harmful bacteria the easy access to iron but, at the same time, limits available iron for the plant itself as well as beneficial bacteria. However, limiting iron availability in the rhizosphere generally might contain the risk for promoting the virulence of bacteria found in the rhizosphere, if it resembles the situation in the mammalian gut, where metabolic cooperativity and iron levels have been shown to suppress virulence³⁷.

A close linkage of nutrient stress response and the plant immune system has been observed for plant responses to phosphate^{38–40} and points towards a general and complex intertwining of nutrient acquisition and plant immune responses. For the conduit between iron and the immune system, IMAs appear to be a key component mediating a set of complex and multifaceted functions. On one hand, IMA local degradation allows for shutting down root acidification, thereby enabling root responses to flg22, such as growth arrest and full phosphorylation of MAPKs. Consistent with these data, a lack of IMA led to less colonization of the root with a surface-dwelling commensal bacteria strain. On the other hand, IMA1-overexpressing plants were more resistant to foliar *P. syringae* pv. tomato DC3000. It will be interesting to explore in the future the extent to which modulation of iron acquisition and storage affects microbiome composition and microbial virulence in the roots and shoots of plants.

Online content

Any methods, additional references, Nature Portfolio reporting summaries, source data, extended data, supplementary information,

acknowledgements, peer review information; details of author contributions and competing interests; and statements of data and code availability are available at <https://doi.org/10.1038/s41586-023-06891-y>.

1. Yilmaz, B. & Li, H. Gut microbiota and iron: the crucial actors in health and disease. *Pharmaceutics* **https://doi.org/10.3390/ph11040098** (2018).
2. Seyoum, Y., Baye, K. & Humblot, C. Iron homeostasis in host and gut bacteria—a complex interrelationship. *Gut Microbes* **13**, 1–19 (2021).
3. Harbort, C. J. et al. Root-secreted coumarins and the microbiota interact to improve iron nutrition in *Arabidopsis*. *Cell Host Microbe* **28**, 825–837 (2020).
4. Stringlis, I. A. et al. MYB72-dependent coumarin exudation shapes root microbiome assembly to promote plant health. *Proc. Natl Acad. Sci. USA* **115**, E5213–E5222 (2018).
5. Ganz, T. & Nemeth, E. Iron homeostasis in host defence and inflammation. *Nat. Rev. Immunol.* **15**, 500–510 (2015).
6. Robinson, N. J., Procter, C. M., Connolly, E. L. & Guerinot, M. L. A ferric-chelate reductase for iron uptake from soils. *Nature* **397**, 694–697 (1999).
7. Eide, D., Broderius, M., Fett, J. & Guerinot, M. L. A novel iron-regulated metal transporter from plants identified by functional expression in yeast. *Proc. Natl Acad. Sci. USA* **93**, 5624–5628 (1996).
8. Vert, G. G. et al. IRT1, an *Arabidopsis* transporter essential for iron uptake from the soil and for plant growth. *Plant Cell* **14**, 1223–1233 (2002).
9. Schmidt, W., Michalke, W. & Schikora, A. Proton pumping by tomato roots. Effect of Fe deficiency and hormones on the activity and distribution of plasma membrane H⁺-ATPase in rhizodermal cells. *Plant Cell Environ.* **26**, 361–370 (2003).
10. Hentze, M. W., Muckenthaler, M. U., Galy, B. & Camaschella, C. Two to tango: regulation of mammalian iron metabolism. *Cell* **142**, 24–38 (2010).
11. Brown, J. C. Iron chlorosis in plants. *Adv. Agron.* **13**, 329–369 (1961).
12. Romera, F. J. et al. Induced systemic resistance (ISR) and Fe deficiency responses in dicot plants. *Front. Plant Sci.* **10**, 287 (2019).
13. Zamioudis, C. et al. Rhizobacterial volatiles and photosynthesis-related signals coordinate MYB72 expression in *Arabidopsis* roots during onset of induced systemic resistance and iron-deficiency responses. *Plant J.* **84**, 309–322 (2015).
14. Aznar, A., Pariat, O., Berger, A. & Dellagi, A. Alterations of iron distribution in *Arabidopsis* tissues infected by *Dickeya dadantii*. *Mol. Plant Pathol.* **16**, 521–528 (2015).
15. Xing, Y. et al. Bacterial effector targeting of a plant iron sensor facilitates iron acquisition and pathogen colonization. *Plant Cell* **33**, 2015–2031 (2021).
16. Nobori, T. et al. Transcriptome landscape of a bacterial pathogen under plant immunity. *Proc. Natl Acad. Sci. USA* **115**, E3055–E3064 (2018).
17. Gu, S. et al. Competition for iron drives phytopathogen control by natural rhizosphere microbiomes. *Nat. Microbiol.* **5**, 1002–1010 (2020).
18. Meziane, H., I, V. D. S., LC, V. A. N. L., Höfte, M. & Bakker, P. A. Determinants of *Pseudomonas putida* WCS358 involved in inducing systemic resistance in plants. *Mol. Plant Pathol.* **6**, 177–185 (2005).
19. Verbon, E. H. et al. Iron and immunity. *Ann. Rev. Phytopathol.* **55**, 355–375 (2017).
20. Platre, M. P. et al. The receptor kinase SRF3 coordinates iron-level and flagellin-dependent defense and growth responses in plants. *Nat. Commun.* **13**, 4445 (2022).
21. Colangelo, E. P. & Guerinot, M. L. The essential basic helix-loop-helix protein FIT1 is required for the iron deficiency response. *Plant Cell* **16**, 3400–3412 (2004).
22. Grillet, L., Lan, P., Li, W., Mokkapati, G. & Schmidt, W. IRON MAN is a ubiquitous family of peptides that control iron transport in plants. *Nat. Plants* **4**, 953–963 (2018).
23. Kroh, G. E. & Pilon, M. Connecting the negatives and positives of plant iron homeostasis. *N. Phytol.* **223**, 1052–1055 (2019).
24. Ngou, B. P. M., Ahn, H.-K., Ding, P. & Jones, J. D. G. Mutual potentiation of plant immunity by cell-surface and intracellular receptors. *Nature* **592**, 110–115 (2021).
25. Yuan, M. et al. Pattern-recognition receptors are required for NLR-mediated plant immunity. *Nature* **592**, 105–109 (2021).
26. Dubeaux, G., Neveu, J., Zelazny, E. & Vert, G. Metal sensing by the IRT1 transporter-receptor orchestrates its own degradation and plant metal nutrition. *Mol. Cell* **69**, 953–964 (2018).
27. Martin-Barranco, A., Spielmann, J., Dubeaux, G., Vert, G. & Zelazny, E. Dynamic control of the high-affinity iron uptake complex in root epidermal cells. *Plant Physiol.* **184**, 1236–1250 (2020).
28. Faulkner, C. et al. LYM2-dependent chitin perception limits molecular flux via plasmodesmata. *Proc. Natl Acad. Sci. USA* **110**, 9166–9170 (2013).
29. Vatén, A. et al. Callose biosynthesis regulates symplastic trafficking during root development. *Dev. Cell* **21**, 1144–1155 (2011).
30. Li, Y. et al. IRON MAN interacts with BRUTUS to maintain iron homeostasis in *Arabidopsis*. *Proc. Natl Acad. Sci. USA* **118**, e2109063118 (2021).
31. Rodriguez-Celma, J. et al. *Arabidopsis* BRUTUS-LIKE E3 ligases negatively regulate iron uptake by targeting transcription factor FIT for recycling. *Proc. Natl Acad. Sci. USA* **116**, 17584–17591 (2019).
32. Liu, L. et al. Extracellular pH sensing by plant cell-surface peptide-receptor complexes. *Cell* **185**, 3341–3355 (2022).
33. Yu, K. et al. Rhizosphere-associated *Pseudomonas* suppress local root immune responses by gluconic acid-mediated lowering of environmental pH. *Curr. Biol.* **29**, 3913–3920 (2019).
34. Liu, Y. et al. Plant commensal type VII secretion system causes iron leakage from roots to promote colonization. *Nat. Microbiol.* <https://doi.org/10.1038/s41564-023-01402-1> (2023).
35. Verbon, E. H. et al. Rhizobacteria-mediated activation of the Fe deficiency response in *Arabidopsis* roots: impact on Fe status and signaling. *Front. Plant Sci.* <https://doi.org/10.3389/fpls.2019.00909> (2019).
36. Zhou, F. et al. Co-incidence of damage and microbial patterns controls localized immune responses in roots. *Cell* **180**, 440–453 (2020).
37. Sanchez, K. K. et al. Cooperative metabolic adaptations in the host can favor asymptomatic infection and select for attenuated virulence in an enteric pathogen. *Cell* **175**, 146–158 (2018).
38. Hiruma, K. et al. Root endophyte *Colletotrichum tofieldiae* confers plant fitness benefits that are phosphate status dependent. *Cell* **165**, 464–474 (2016).
39. Castrillo, G. et al. Root microbiota drive direct integration of phosphate stress and immunity. *Nature* **543**, 513–518 (2017).
40. Dindas, J. et al. Direct inhibition of phosphate transport by immune signaling in *Arabidopsis*. *Curr. Biol.* **32**, 488–495 (2022).

Publisher's note Springer Nature remains neutral with regard to jurisdictional claims in published maps and institutional affiliations.

Springer Nature or its licensor (e.g. a society or other partner) holds exclusive rights to this article under a publishing agreement with the author(s) or other rightsholder(s); author self-archiving of the accepted manuscript version of this article is solely governed by the terms of such publishing agreement and applicable law.

© The Author(s), under exclusive licence to Springer Nature Limited 2024

Methods

Plant material and plant growth conditions

For all of the experiments, *Arabidopsis thaliana* ecotype Columbia (Col-0) was used as the WT control. Plant seeds were sterilized in 70% ethanol for 8 min and washed with sterilized MilliQ water. Seeds were sowed on agar medium and stratified at 4 °C for 3 days in the dark. Seedlings were grown in a Percival growth chamber (Geneva Scientific) at 22 °C under a 16 h–8 h light–dark cycle. Iron-sufficient (+Fe) medium was prepared according to the recipe of standard medium as described previously⁴¹. The medium contains: 750 µM of MgSO₄·7H₂O, 625 µM of KH₂PO₄, 1,000 µM of NH₄NO₃, 9,400 µM of KNO₃, 1,500 µM of CaCl₂·2H₂O, 0.055 µM of CoCl₂·6H₂O, 0.053 µM of CuCl₂·2H₂O, 50 µM of H₃BO₃, 2.5 µM of KI, 50 µM of MnCl₂·4H₂O, 0.52 µM of Na₂MoO₄·2H₂O, 15 µM of ZnCl₂, 75 µM of Na-Fe-EDTA (+Fe) or 10 µM of Na-Fe-EDTA (phenotype analysis), 1,000 µM of 2-(N-morpholino)ethanesulfonic (MES) adjusted to pH 5.5 with KOH, 0.5% sucrose and 1% Difco Agar (BD, 214530, only for seedling growth on solid medium).

Generation of transgenic lines

To generate the transgenic plants with *IMA1* driven by different promoters, the upstream promoter region based on the previous study⁴² of *UBQ10* (AT4G05320, 1,986 bp), *PGP4* (AT2G47000, 2,174 bp), *ELTP* (At2g48140, 464 bp) and *LBD16* (AT2G42430, 2,564 bp) was cloned into p5' (pDONR P4-P1r), the *mCitrine* coding sequence without the stop codon was cloned into p221 (pDONR 221) and the *IMA1* coding sequence with stop codon was cloned into p3' (pDONR P2r-P3) through BP reactions. The destination construct was combined using pB7m34GW, p221-mCitrine, p3'-IMA1 and one of the p5' vectors using the multiple-gateway LR reaction. The destination constructs were transformed into Col-0 and selected on the basis of Basta resistance to obtain homozygous T3 transgenic lines. To generate *pIMA1::mCitrine-NLS-mCitrine*, the same promoter region of *pIMA1::eYFP-IMA1;ima8x* used in a previous study²² was cloned into p5' (pDONR P4-P1r) through BP reactions. The destination construct was combined using pB7m34GW, p221-mCitrine, p3'-NLS-mCitrine and p5'-IMA1pro using the multiple-gateway LR reaction. The destination constructs were transformed into Col-0 and selected on the basis of Basta resistance to obtain homozygous T3 transgenic lines. To generate *pIMA1::eYFP-IMA1* plants in the *bts-1, fls2* and *bts1, l2* mutant background, *pIMA1::eYFP-IMA1;ima8x* was crossed to *bts-1, fls2* and *bts1, l2* mutants, respectively, and the F₃ homozygous transgenic plants were obtained for experimental analysis.

Elicitor preparation and treatment

Flg22 oligopeptide (QRLSTGSRINSAKDDAAGLQIA) and flg20 oligopeptide (QRLSTGSRINSAKDDAAGLQ) were synthesized by the Salk Peptide Synthesis Core. The elf18 oligopeptide (Ac-SKEKFERTKPHVNVTIG) was obtained from EZBiolab. The peptides were dissolved in deionized water. Chitin (Frontier Scientific, JK399372) was dissolved in deionized water at 4 °C with overnight rotating.

For elicitor treatment, flg22 and flg20 were added to the liquid medium to obtain the respective final concentration (depending on the time scale of the assay 2 µM, 1 µM, 100 nM or 10 nM as described in the figure legends). Chitin was diluted to 1 mg ml⁻¹ as the final concentration. Seedlings were treated in +Fe (75 µM FeEDTA) or -Fe (0 µM FeEDTA, 50 µM FerroZine (ACROS Organics, 410570050)) liquid medium containing the elicitors for 24 h, unless otherwise specified.

Protein extraction and western blotting

Seedlings (aged 7 days) grown on +Fe plates were transferred to liquid medium with +Fe (75 µM Fe), +Fe + flg22 (75 µM Fe + 100 nM flg22), -Fe (50 µM FerroZine), -Fe + flg22 (50 µM FerroZine + 100 nM flg22) and treated for 24 h. For the protein extraction and western blot procedure, a previously published method was used with minor modifications⁴³.

For IRT1 and eYFP-IMA1 detection, 15 roots cut from the pretreated seedlings were harvested immediately in liquid nitrogen. The samples were ground with liquid nitrogen and lysed directly in 80 µl total protein extraction buffer (50 mM Tris-Cl pH 7.4, 150 mM NaCl, 5 mM EDTA, 1% SDS and 1% Triton X-100 supplemented with 1× NuPAGE LDS sample buffer (Invitrogen, NP0008) and 1× NuPAGE sample reducing agent (Invitrogen, NP0009) for 15 min on ice. The protein samples were denatured by heating for 10 min at 90 °C and centrifuged at 13,000 rpm for 10 min. The supernatant protein samples were separated on a NUPAGE 10% Bis-Tris Plus Gel (Invitrogen, NW00105BOX) and transferred onto a nitrocellulose membrane by the iBlot 2 Dry Blotting system (Invitrogen, IB23001). IRT1 was detected by western blotting with corresponding antibody (primary antibody, anti-IRT1 (Agrisera, AS111780) 1:2,000 diluted in 5% non-fat milk; secondary antibody: goat anti-rabbit IgG (H+L)-HRP conjugate (Bio-Rad, 170-6515) 1:5,000 in 5% non-fat milk). eYFP-IMA1, mCitrine-IMA1 and free GFP expressed in CHAO bacteria were detected using the anti-GFP HRP conjugate antibody (Miltenyi Biotec, 130-091-833, 1:2,000 diluted in 5% non-fat milk). FIT-3×HA was detected using the anti-HA HRP conjugate antibody (Roche, 12013819001, 1:2,000 diluted in 5% non-fat milk). The same membrane was stripped by the following steps (1) wash the membrane with 1 M NaOH for 5 min and then (2) wash the membrane three times with 1× TBST for 5 min. Then, the membrane was reblotted with anti-tubulin antibodies as the internal control (Invitrogen, 32-2500, 1:5,000 in 5% non-fat milk; goat anti-mouse IgG (H+L)-HRP conjugate (Bio-Rad, 170-6516), 1:5,000 in 5% non-fat milk).

Western blot analysis of MAPK activity

A total of 20 seedlings of the 7-day-old light-grown Col-0 and *UBQ10::mCitrine-IMA1* lines on the +Fe plates without MES were treated in Fe-sufficient liquid medium without MES with 1 µM flg22 peptide for 5 and 10 min. The root and shoot parts of the seedlings were harvested separately and the samples were then ground with liquid nitrogen and lysed directly in 80 µl (for root samples) or 150 µl (for shoot samples) total protein extraction buffer (same as described above). The phosphorylation status of MPK3 and MPK6 was detected by western blotting with the corresponding antibodies (phospho-P44/42 MAPK antibodies (Cell Signaling, 4370) 1:2,000 diluted in 1% BSA, Merck/Calbiochim, 12657; goat anti-rabbit IgG (H+L)-HRP conjugate (Bio-Rad, 170-6515) 1:5,000 in 5% non-fat milk). The same membrane was reblotted with anti-tubulin antibodies (root samples) (Invitrogen, 32-2500, 1:5,000 in 5% non-fat milk; goat anti-mouse IgG (H+L)-HRP conjugate (Bio-Rad, 170-6516), 1:5,000 in 5% non-fat milk as an internal control).

FCR activity measurement

Seedlings (aged 7 days) grown on +Fe plates were transferred to liquid medium with +Fe (75 µM Fe), +Fe + flg22 (75 µM Fe + 100 nM flg22), -Fe (50 µM FerroZine) or -Fe + flg22 (50 µM FerroZine + 100 nM flg22) and treated for 2 days. The seedlings were washed with deionized water five times to remove any residual chemicals and 8–10 seedlings were pooled as one sample. The seedlings were incubated in the assay solution containing 0.1 mM Fe(III)-EDTA and 0.3 mM FerroZine in the dark for 1 h. The FCR activity was measured by spectrophotometry (Beckman Coulter, DU 730) with the absorbance (562 nm) of the Fe(II)-FerroZine complex. The results were calculated on a root FW using the following formula:

$$\text{FCR activity (nmol (g h)⁻¹)} = \text{OD}_{562}/29,800 \times V(\text{ml})/\text{FW (g)} / T(\text{h}) \times 10^6$$

Total chlorophyll concentration measurement

The total chlorophyll content measurement was determined using spectrophotometry analysis. In brief, four shoots of the plants were harvested and pooled as one sample. Any liquid was carefully removed from the sample before the FW was measured. Chlorophyll was extracted with 80% acetone in TissueLyser until the pellet became white. The leaf

extracts were measured by spectrophotometry (Beckman Coulter, DU 730, 1 cm width cuvettes) with absorbances of 663 nm and 647 nm for chlorophyll *a* and *b*, respectively. The results were calculated on a root fresh-weight basis as follows:

$$\text{Total chlorophyll } (a+b) \text{ } (\mu\text{g ml}^{-1}) = (7.15 \times A_{663}) + (18.71 \times A_{647}).$$

Total chlorophyll concentration = (total chlorophyll \times extract volume (ml)) / FW (g).

Iron concentration measurement

The total iron content was measured using a spectrophotometry method that was described previously⁴⁴. The seedlings were harvested and rinsed with deionized water five times and dried in an oven at 65 °C for 2 days. After measuring the DW, the tissues were digested with 65% (v/v) HNO₃ at 95 °C for 6 h, followed by adding 30% (v/v) H₂O₂ at 56 °C for 2 h. The iron content was analysed in the assay solution (1 mM bathophenanthroline disulfonate (BPDS), 0.6 M sodium acetate and 0.48 M hydroxylamine hydrochloride). The FeCl₃ solution was used to prepare the standard curve. The resulting Fe²⁺-BPDS₃ complex was measured with absorbance (535 nm) using a microplate reader. The iron content in each sample was calculated by the absorbance values against the standard curve and normalized by the DW.

Confocal microscopy for *pIRT1::NLS-2xYPet* and *pIMA1::eYFP-IMA1* with PI staining

Seedlings were precultured on +Fe (75 μM Fe) solid medium for 4 days. For the treatment, around 8–10 seedlings were transferred to 5 ml of +Fe (75 μM Fe), +Fe + flg22 (75 μM Fe + 100 nM flg22), -Fe (50 μM FerroZine) and -Fe + flg22 (50 μM FerroZine + 100 nM flg22) liquid medium in a six-well plate and treated for 24 h. For PI staining, pretreated seedlings were stained with PI solution (2 μg ml⁻¹, dissolved in MilliQ water) for 5 min and rinsed in water. Imaging experiments were performed on the Zeiss LSM710 confocal microscope with a C-Apochromat $\times 40/1.20$ W Korr M27 water objective lens. Ypet was excited with a 488 nm laser and fluorescence emission was filtered by a 505/550 nm filter. The PI signal was excited with either 488 or 514 nm laser and fluorescence emission was filtered by a 600/650 nm filter. For the quantification of the raw intensity of the Ypet signal, the process was automated using the Fiji macro, MACRO_Min_pIRT1_LSM710_PI-staining.

For eYFP-IMA1 imaging in the leaf, 4-day-old *pIMA1::eYFP-IMA1;ima8x* seedlings were incubated in 5 ml of +Fe (75 μM Fe), +Fe + flg22 (75 μM Fe + 100 nM flg22), -Fe (50 μM FerroZine) and -Fe + flg22 (50 μM FerroZine + 100 nM flg22) liquid medium in a six-well plate for 24 h. Before imaging, cotyledons were excised and mounted in water, abaxial side of epidermis, mesophyll and vasculature regions were imaged using the C-Apochromat $\times 40/1.20$ W Korr M27 water objective lens. The bright field was imaged at the same time as the control. YFP was excited with a 514 nm laser and fluorescence emission was filtered by a 520/570 nm filter.

Microscopy set-up for eYFP-IMA1 quantification

Imaging experiments except when indicated below were performed using the following Zeiss LSM710 confocal microscope set up: inverted Zeiss microscope using a Plan-Apochromat $\times 20/0.8$ M27 objective lens. YFP was excited with a 514 nm laser (60 mW) and fluorescence emission was filtered by a 519/580 nm filter.

Calculation of the eYFP-IMA1 mean grey values

Eight z-stack images were acquired in bright field and eYFP signal representing a root section between 35 and 45 μm. The bright-field images were processed with a z-projection using the standard deviation method. From these images, the root area was detected using the plugin Wavelet a trou (<http://www.ens-lyon.fr/RDP/SiCE/METHODS.html>)⁴⁵. The eYFP images were processed with a z-projection using the sum method. On those images, the root area that was previously determined was reported and the mean grey value was measured in this area

to obtain the mean grey value of the eYFP channel. The process has been automatized using the Fiji software Macro, MACRO_Intensity_IMA1.

Calculation of the eYFP-IMA1 diameter

Eight z-stack images were acquired in bright field and eYFP signal representing a section between 35 and 45 μm. The bright-field images were processed with a z-projection using standard deviation method. The eYFP images were processed with a z-projection using the sum method. In Fiji, the root width was calculated using the straight line and, on the same zone, the width of the eYFP signal was determined. The ratio of the eYFP width was divided by the root width and multiplied by 100 to obtain the percentage of eYFP-IMA1 tissue lateral diffusion.

Rhizosphere acidification assay and pH quantification

Col-0, *ima8x* and *UBQ10::mCitrine-IMA1* seedlings were precultured on +Fe (75 μM Fe) solid medium for 7 days. The seedlings were transferred to +Fe solid medium or no Fe (0 μM Fe, 50 μM FerroZine) solid medium for 3 days before the pH assay was performed. The seedlings were then placed onto a 1% agar plate containing 0.05% (w/v) bromocresol purple (pH 6.5 adjusted with NaOH) for 24 h before being photographed.

Quantification of rhizosphere pH was conducted with a spectrophotometric assay that was published with some modification^{46,47}. Seedlings (aged 7 days) grown on +Fe plates without MES were transferred to liquid medium with +Fe (75 μM Fe), +Fe + flg22 (75 μM Fe + 100 nM flg22), -Fe (50 μM FerroZine) or -Fe + flg22 (50 μM FerroZine + 100 nM flg22) without MES and treated for 2 days. The seedlings were then transferred to the same liquid medium supplemented with the pH indicator bromocresol purple (0.005%) for 1 day in 48-well plates. Proton extrusion capacity was analysed by reading the absorption at 590 nm (A_{590}) using an automated microplate reader.

CHA0 bacterial strain growth condition and inoculation

The GFP- and mCherry-labelled *P. protegens* strains CHAO-gfp2 (CHAO::attTn7-gfp2; Gm^r) and CHAO-mCherry (CHAO::attTn7-mCherry; Gm^r) were used for the bacteria inoculation assay³⁶. The CHAO-gfp2 or CHAO-mCherry strain was cultured in liquid LB medium (Miller's LB Broth, Research products international, L24040) supplemented with 25 μg ml⁻¹ gentamycin at 28 °C overnight. Bacteria cells were collected by centrifugation (1 min, 5,000 rpm) and resuspended in sterile MilliQ water five times to prevent potential element contamination from the LB medium.

For the bacteria inoculation experiment, 4-day-old seedlings (imaging for IMA1 in the differentiation zone) or 7-day-old seedlings (imaging for IMA1 in the LRP) that were precultured on +Fe (75 μM Fe) solid medium were treated with liquid medium. Around 8–10 seedlings were transferred to 5 ml (Gruber medium with 0.25% sucrose) of +Fe (75 μM Fe), +Fe + CHAO (75 μM Fe + CHAO-gfp2 or CHAO-mCherry), -Fe (100 μM FerroZine), -Fe + CHAO (100 μM FerroZine + CHAO-gfp2 or CHAO-mCherry) and -Fe + flg22 (100 μM FerroZine + 100 nM flg22) liquid medium in a six-well plate and treated for 24 h. For the liquid treatment with CHAO, the bacterial suspension was added in the well to a final optical density at 600 nm (OD₆₀₀) of 0.05.

Analysis of the effect of iron on CHAO colonization of *Arabidopsis* roots was performed according to the previous studies with some modification^{3,34,36}. In brief, seedlings (aged 7 days) of Col-0, *ima8x* and *UBQ10::mCitrine-IMA1* were transferred to 5 ml (Gruber medium without MES and sucrose) of +Fe (50 μM FeEDTA pH 5.5), -Fe (100 μM FerroZine) or non-available iron (nAvFe 50 μM FeCl₃ with pH 7.0) liquid medium in a six-well plate and treated for 24 h with prewashed CHAO-mCherry at a final OD₆₀₀ of 0.02. After the treatment, the roots were gently washed with sterilized deionized water to remove the non-attached bacteria and the root length was measured. The roots were harvested in 1 ml extraction buffer (10 mM MgCl₂, 0.01% Silwet L-77) and homogenized using TissueLyser with stainless steel beads.

Article

The samples were diluted serially from 10^1 to 10^6 , and then spread onto LB agar plates supplemented with $30 \mu\text{g ml}^{-1}$ gentamycin. The colony-forming units (CFUs) were counted after 30 h incubation at 28°C . The calculated CFUs were normalized to the root length.

P. syringae pv. *tomato* DC3000 infection assay

A. thaliana Col-0 and *UBQ10::mCitrine-IMA1* were grown in a chamber at 22°C under a 12 h light period and 60–70% relative humidity for 30–31 days in the soil. *P. syringae* pv. *tomato* DC3000 was cultured in King's B (KB) liquid medium with antibiotics (rifampicin and tetracycline) at 28°C . Bacteria were collected by centrifugation and resuspended in sterile water to an OD_{600} of 0.001 (approximately 5×10^6 CFU per ml). *A. thaliana* leaves (2–3 fully expanded leaves per plant) were infiltrated with bacterial suspensions using a needleless syringe. Then, 2 days after bacterial infiltration, two leaf discs (0.13 cm^2) per leaf were homogenized in 200 μl of MgSO_4 , and a dilution series was streaked onto KB plates. The plates were incubated at 28°C for approximately 2 days before CFUs were counted.

RT-qPCR

Seedlings (aged 7 days) grown on +Fe solid medium were transferred to 5 ml +Fe, +Fe + flg22, -Fe and -Fe + flg22 liquid medium in a six-well plate and treated for 24 h unless otherwise specified. The root total RNA was isolated from around 15 roots (as a pool for one biological replicate) using the Spectrum Plant Total RNA Kit (Sigma-Aldrich, STRN250). A total of 500 ng of total RNA was reverse-transcribed to cDNA using the Maxima H Minus cDNA Synthesis Master Mix with dsDNase (Thermo Fisher Scientific, M1682). RT-qPCR was performed using the Bio-Rad CFX384 Real-Time System and Luna qPCR mix (New England Biolabs, M3003L) according to the manufacturer's instructions. A list of all of the primers used for RT-qPCR analysis is provided in Supplementary Table 1.

RNA-seq and data analysis

For transcriptomic analysis, 7-day-old seedlings grown on +Fe medium plates were transferred to 5 ml +Fe, +Fe + flg22, -Fe and -Fe + flg22 liquid medium in a six-well plate and treated for 24 h. In total, 20 roots were harvested, pooled as one biological replicate, with a total of three independent replicates per condition in each genotype (total sample number = 36). The root samples were ground in liquid nitrogen and the RNA was extracted using the Spectrum Plant Total RNA Kit (Sigma-Aldrich, STRN250). The RNA quality and quantity were determined using the 2100 Bioanalyzer and TapeStation (Agilent Technologies) and the Qubit Fluorometer (Invitrogen). The sequencing libraries were generated using the Salk Next Generation Sequencing Core according to Illumina manufacturer's instructions. Sequencing was performed using the Illumina NextSeq 2000 platform.

Read alignment and generation of counts

RNA-seq short reads were mapped to the TAIR 10 reference genome which were obtained from the Arabidopsis Information resource web site (<http://www.arabidopsis.org>)⁴⁸ using the Splice Transcripts Alignments to Reference (STAR) (v.2.7.0a)⁴⁹. A STAR index was built using the following parameters before mapping:

```
$ STAR --runThreadN 4 \
--runMode genomeGenerate \
--genomeDir ara_star_index \
--genomeFastAFiles <TAIR10.fa> \
--sjdbGTFfile <TAIR10.gtf> \
--sjdbOverhang 99
```

Then, RNA-seq reads in the FASTQ files were aligned to TAIR 10 and raw count files were generated using the following STAR command:

```
$ STAR --genomeDir ara_star_index \
--runThreadN 8 \
--sjdbOverhang 99 \
```

```
--sjdbGTFfile <TAIR10.gtf> \
--outSAMtype BAM SortedByCoordinate \
--outFileNamePrefix /output/small_ \
--outReadsUnmapped Fastx \
--quantMode GeneCounts \
--readFilesIn <fastq>
```

A custom R script (`min_R_codes_for_manuscript`) was used to combine counts per gene from count data produced from STAR cross all of the samples.

Differential expression analysis

Normalization of the read counts and differential gene expression analysis were performed using the R package edgeR (v.3.36.0)⁵⁰. The CPM function from edgeR was used to normalize the gene expression. The DEGs were identified using glmLRT function from edgeR. False-discovery rate (FDR < 0.05) and log-transformed fold change (>0 or <0) were used as the criteria values for identification of upregulated and downregulated DEGs.

The DEG analysis was conducted by comparing different combinations of iron and flg22 treatments in the WT using ANOVA with Benjamini-Hochberg correction (FDR < 0.05) plus the maximal absolute value of \log_2 -converted fold change between pairs of treatment conditions larger than 1. DEGs were visualized and the k-means clustering method was used to classify DEGs using the ComplexHeatmap⁵¹ package in R. The cluster number ($k = 5$) was determined by the total within-cluster sum of the squared error and Bayesian information criterion. The box plots were used to display scaled expression of genes from each cluster.

GO enrichment analysis was conducted using online tools of the GO website (<http://geneontology.org/>).

Statistical analysis

Statistical significance of overlap between DEGs from was assessed using hypergeometric distribution tests. The Hypergeometric test function in R was used to calculate statistical significance with the following parameters: `$ hyper(q-1, m, n-m, k, lower.tail = FALSE, log.p = FALSE)`, where q is the number of genes in common between two sets, m is the number of genes in set 1; n is the total number of genes in the RNA-seq counts table (33,602) and k is the number of genes in set 2.

Statistical analysis was performed using GraphPad Prism 9 and XLSTAT (v.2020.4.1.1032).

Box and whisker plots

For all of the box and whisker plots (unless specified in the figure legend), the upper and lower boundary show the minimum to maximum values. The horizontal line in the box represents the median value. The upper quartile represents 75th percentile and the lower quartile represents 25th percentile.

Statistics and reproducibility

Each experiment was repeated independently least three times with consistent results, except for the western blot in Fig. 3g, which was repeated twice showing consistent results.

Reporting summary

Further information on research design is available in the Nature Portfolio Reporting Summary linked to this article.

Data availability

Raw RNA-seq data have been uploaded to the NCBI Gene Expression Omnibus (GSE213557). Uncropped gel and blot source data are provided in Supplementary Fig. 1. Gene sequences for RNA-seq read mapping were obtained from the TAIR10 reference genome. Source data are provided with this paper.

Code availability

Scripts for imaging quantification in Fiji and code for RNA-seq analysis in R are available at GitHub (<https://github.com/cm010713/immunity-iron-project>). All bioinformatic tools used in this study are cited in the Methods.

41. Gruber, B. D., Giehl, R. F. H., Friedel, S. & von Wirén, N. Plasticity of the *Arabidopsis* root system under nutrient deficiencies. *Plant Physiol.* **163**, 161–179 (2013).
42. Wyrtsch, I., Domínguez-Ferreras, A., Geldner, N. & Boller, T. Tissue-specific FLAGELLIN-SENSING 2 (FLS2) expression in roots restores immune responses in *Arabidopsis fls2* mutants. *N. Phytol.* **206**, 774–784 (2015).
43. Cao, M. et al. TMK1-mediated auxin signalling regulates differential growth of the apical hook. *Nature* **568**, 240–243 (2019).
44. Gautam, C. K., Tsai, H.-H. & Schmidt, W. A quick method to quantify iron in *Arabidopsis* seedlings. *Bio Protoc.* **12**, e4342 (2022).
45. Bayle, V., Platret, M. P. & Jajlaia, Y. Automatic quantification of the number of intracellular compartments in *Arabidopsis thaliana* root cells. *Bio Protoc.* <https://doi.org/10.21769/BioProtoc.2145> (2017).
46. Santi, S. & Schmidt, W. Dissecting iron deficiency-induced proton extrusion in *Arabidopsis* roots. *N. Phytol.* **183**, 1072–1084 (2009).
47. Gujas, B., Alonso-Blanco, C. & Hardtke, C. S. Natural *Arabidopsis brx* loss-of-function alleles confer root adaptation to acidic soil. *Curr. Biol.* **22**, 1962–1968 (2012).
48. Berardini, T. Z. et al. The *Arabidopsis* information resource: making and mining the “gold standard” annotated reference plant genome. *Genesis* **53**, 474–485 (2015).
49. Dobin, A. et al. STAR: ultrafast universal RNA-seq aligner. *Bioinformatics* **29**, 15–21 (2012).
50. Robinson, M. D., McCarthy, D. J. & Smyth, G. K. edgeR: a Bioconductor package for differential expression analysis of digital gene expression data. *Bioinformatics* **26**, 139–140 (2010).
51. Gu, Z., Eils, R. & Schlesner, M. Complex heatmaps reveal patterns and correlations in multidimensional genomic data. *Bioinformatics* **32**, 2847–2849 (2016).

Acknowledgements We thank J. Balk for providing genetic materials (*btsl1.2* (*btsl1-1 btsl2-2*), *pBTSL1::GFP* and *pBTSL2::GFP*); L. Grillet and W. Schmidt for providing genetic materials (*ima8x*, *IMAtox* and *pIMA1::EYFP-IMA1;ima8x*); C. Keel for providing bacteria materials (CHAO-gfp2 and CHAO-mCherry); the members of the Salk Peptide Synthesis Core for

synthesizing flg22 and flg20 peptides; the members of the Salk Next Generation Sequencing Core Facility for NGS library preparation and sequencing; and S. Lee, C. Miller and N. Gibbs for comments on the manuscript. This study was funded by the National Institute of General Medical Sciences of the National Institutes of Health (grant number R01GM127759 to W.B.), start-up funds from the Salk Institute for Biological Studies (to W.B.), funds from the Hess Chair in Plant Science (to W.B.), a long-term postdoctoral fellowship (LT0000340/2019 L) by the Human Frontier Science Program Organization to M.P.P., funds from the Taiwan’s Ministry of Science and Technology (grant number 111-2917-I-564-021 to H.-H.T.), funds from the Human Frontiers Science Program (HFSP) Long-term Fellowship (grant number LT000661/2020-L to T.N.). This study was supported by the NGS Core Facility of the Salk Institute with funding from NIH-NCI CCSG: P30 014195, the Chapman Foundation and the Helmsley Charitable Trust. J.R.E. is an investigator of the Howard Hughes Medical Institute. L.A. is supported by a Maria Zambrano postdoctoral fellowship by de Ministerio de Universidades and the European Union—NextGenerationEU. Research at CRAG was supported by grant MCIN/AEI/PID2019-108595RB-I00 funded by MCIN/AEI/10.13039/501100011033, grant TED2021-131457B-I00 funded by MCIN/AEI/10.13039/501100011033 and by the ‘European Union NextGenerationEU/PRTR’, through the ‘Severo Ochoa Programme for Centres of Excellence in R&D’ (CEX2019-000917 funded by MCIN/AEI/10.13039/501100011033), and by the CERCA Pro-gram/Generalitat de Catalunya (N.S.C.).

Author contributions M.C. and W.B. conceived the project. M.C., M.P.P. and W.B. conceived and designed experiments. M.C. conceived and conducted most of the experiments. M.P.P. conducted most of the confocal microscopy experiments and all of the imaging quantification. H.-H.T., T.N. and L.A. provided protocols and conducted the bacterial inoculation experiments. L.Z. performed RNA-seq analysis. Y.C. conducted IMA1 imaging experiments in the shoot. W.H. drew schematics for the manuscript. L.B. participated in the generation of transgenic plants. W.B., N.G., J.R.E. and N.S.C. supervised work and provided funds and resources. M.C. and W.B. wrote and revised the manuscript with input from M.P.P., H.-H.T. and Y.C.

Competing interests The authors declare no competing interests.

Additional information

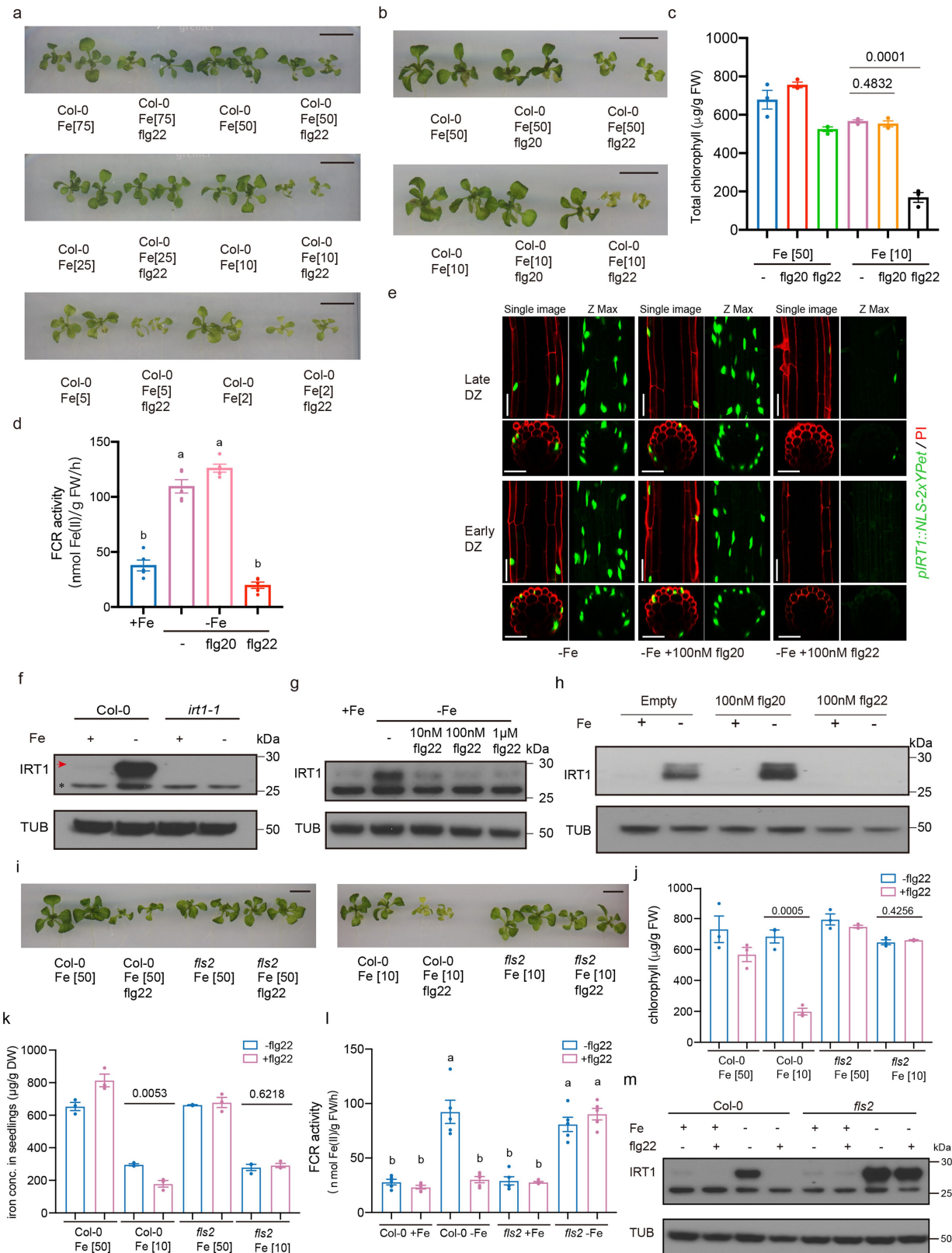
Supplementary information The online version contains supplementary material available at <https://doi.org/10.1038/s41586-023-06891-y>.

Correspondence and requests for materials should be addressed to Wolfgang Busch.

Peer review information *Nature* thanks the anonymous reviewers for their contribution to the peer review of this work.

Reprints and permissions information is available at <http://www.nature.com/reprints>.

Article



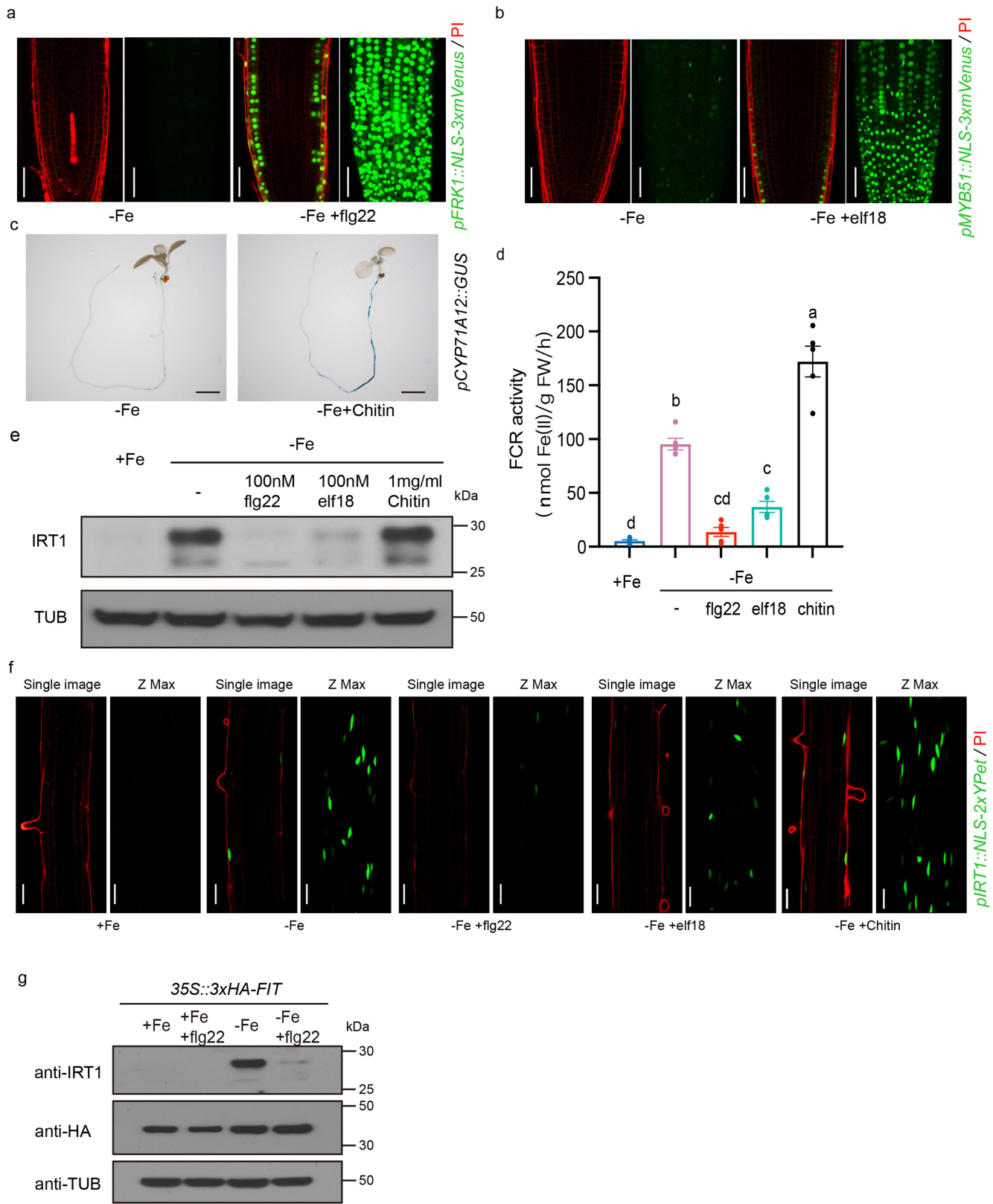
Extended Data Fig. 1 | See next page for caption.

Extended Data Fig. 1 | Flg22 represses iron uptake through FLS2.

a, Phenotype of 15-day-old *Arabidopsis* seedling leaves response to different iron concentrations (shown in figures) with or without low levels of flg22 (10 nM) treatment. Scale bar 1 cm. **b,c**, Phenotype of 15-day-old *Arabidopsis* seedling leaves response to sufficient iron (50 µM) or low iron (10 µM) with or without low levels of flg20 or flg22 (10 nM) treatment. **b**, Shoots; scale bar 1 cm. **c**, Total chlorophyll concentration of Col-0 shoots. Bar chart centres show means of 3 biological replicates. Error bar: s.e.m. The numbers correspond to *p*-values analysed by two-tailed Student t-test. **d**, Quantitative analysis of ferric chelate reductase activities in Col-0 roots grown for 7 days under +Fe conditions and transferred to -Fe, -Fe with flg20 and -Fe with flg22 liquid medium for 2 days. The bar chart centres show means of 5 biological replicates. Error bar: s.e.m. Different letters indicate statistically significant differences between different conditions analysed by one-way ANOVA and Tukey's test (*p* < 0.05). **e**, Promoter activity of *IRT1* in the root of *pIRT1::NLS-2xYpet* seedlings in response to -Fe, -Fe with flg20 and -Fe with flg22 treatment. Seedlings were grown on the +Fe medium and after 5 days transferred to the different liquid media for 24 h treatment. Green: nuclear localized Ypet; red: propidium iodide (PI) cell wall stain. For each treatment, a representative single confocal section (single image, GFP/PI), maximum intensity Z-projection (Z-max, GFP only), a single

optical section of the transverse view, and the Z-projection of the transverse section are shown. Scale bar, 50 µm. **f–h**, Western blots showing IRT1 protein levels in Col-0 and *irt1* roots grown in +Fe and -Fe (**f**) or Col-0 under +Fe, -Fe and -Fe with different concentrations of flg22 treatment (**g**) or Col-0 under +Fe, -Fe and -Fe with flg20 or flg22 treatment (**h**). Arrow indicates the IRT1 protein band. The asterisk indicates non-specific band. Tubulin protein was blotted as an internal control. **i–k**, Phenotype of 15-day-old *Arabidopsis* Col-0 and *fls2* seedling leaves in response to sufficient iron (50 µM) or low iron (10 µM) with or without low levels of flg22 (10 nM) treatment. The numbers correspond to *p*-values that were analysed by two-tailed Student t-test. **i**, Shoots; scale bar 1 cm; **j**, total chlorophyll concentration of Col-0 shoots; **k**, iron concentration of Col-0 seedlings; bar chart centres show means of 3 biological replicates. Error bar: s.e.m. **l**, Quantitative analysis of ferric chelate reductase activities in Col-0 and *fls2* roots grown for 7 days under +Fe conditions and transferred to +Fe, +Fe with flg22, -Fe and -Fe with flg22 liquid medium for 2 days. The bar chart centres show means of 5 biological replicates. Error bar: s.e.m. Different letters indicate statistically significant differences between different conditions analysed by one-way ANOVA and Tukey's test (*p* < 0.05). **m**, Western blots showing IRT1 protein levels in Col-0 and *fls2* roots in +Fe, +Fe with flg22, -Fe and -Fe with flg22 treatment. The tubulin protein was blotted as an internal control.

Article

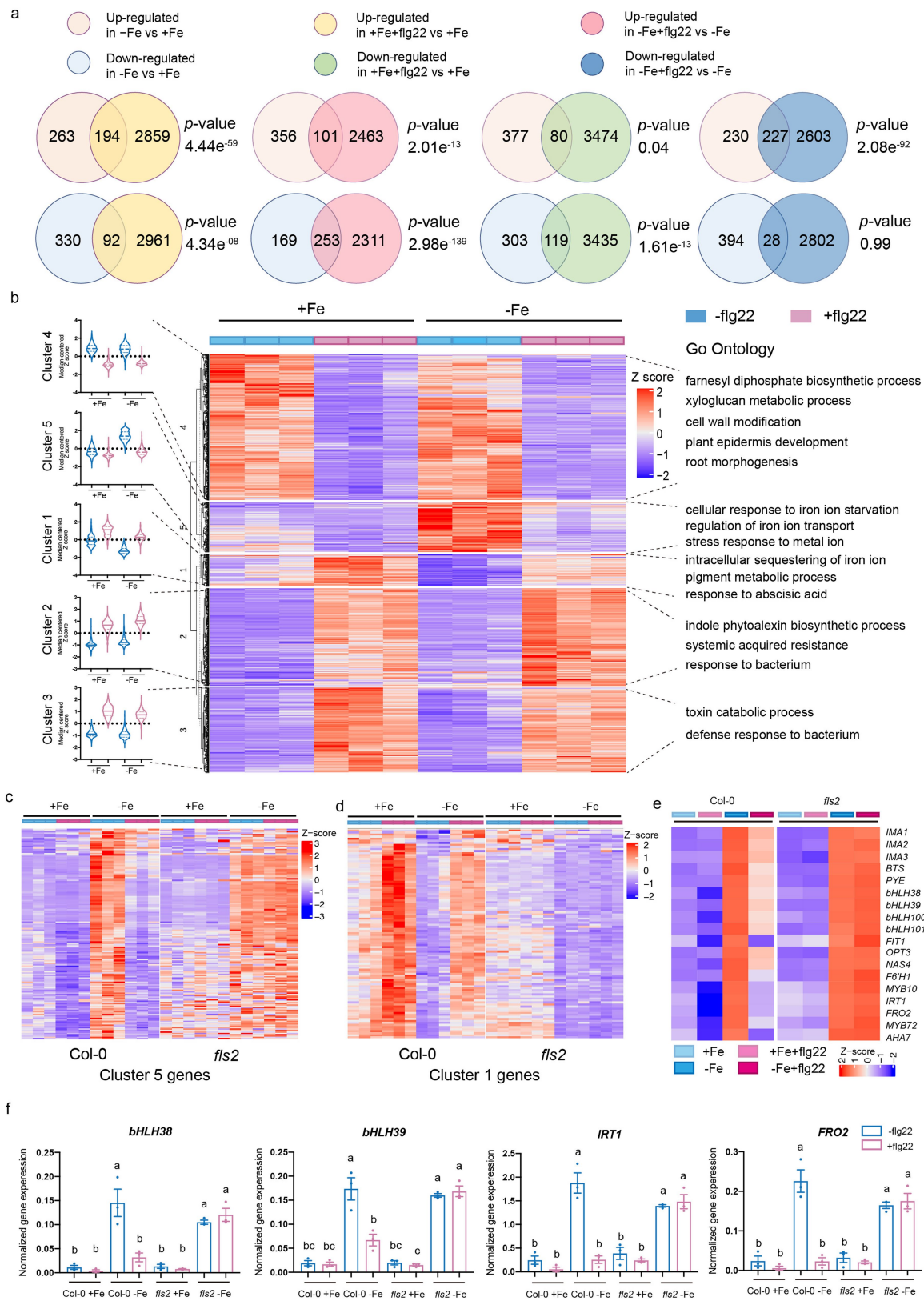


Extended Data Fig. 2 | See next page for caption.

Extended Data Fig. 2 | MAMPs regulate iron uptake through distinct mechanisms. **a,b**, Promoter activity of *FRK1* in roots of *pFRK1::NLS-3xmVenus* seedlings in response to -Fe and -Fe with flg22 treatment (**a**) or promoter activity of *MYB51* in roots of *pMYB51::NLS-3xmVenus* seedlings in response to -Fe and -Fe with elf18 treatment (**b**). 7-day-old seedlings are treated with -Fe and -Fe with 100 nM flg22 (**a**) or -Fe and -Fe with 100 nM elf18 (**b**) for 24 h in liquid media. Green: nuclear localized mVenus signals; red: propidium iodide (PI) cell wall stain. In each treatment, a representative single confocal section (single image, GFP/PI) and Maximum Intensity Z-Projection (Z-max, GFP only) is shown. Scale bar, 50 μ m. **c**, Promoter activity of *CYP71A12* in roots of *pCYP71A12::GUS* seedlings in response to -Fe and -Fe with chitin treatment. 7-day-old seedlings are treated with -Fe and -Fe with 1 mg/mL chitin for 24 h in liquid media. Scale bar, 0.5 cm. **d**, Quantitative analysis of ferric chelate reductase activities in Col-0 roots grown for 7 days under +Fe conditions and transferred to -Fe, -Fe

only or -Fe with flg22, elf18 and chitin liquid medium for 2 days. The bar chart centres show means of 5 biological replicates. Error bars, s.e.m. Different letters indicate statistically significant differences between different conditions analysed by one-way ANOVA and Tukey's test ($p < 0.05$). **e**, Western blots showing IRT1 protein levels in Col-0 roots grown +Fe, -Fe only or -Fe with flg22, elf18 and chitin treatment. Tubulin protein was blotted as an internal control. **f**, Promoter activity of *IRT1* in the root of *pIRT1::NLS-2xYpet* seedlings in response to -Fe only or -Fe with flg22, elf18 and chitin treatment. Green: nuclear localized Ypet signals; red: propidium iodide (PI) cell wall stain. In each treatment, the Z-stack scan is processed to single confocal section (single image, GFP/PI), maximal Z-projection (Z-max, GFP only). Scale bar, 50 μ m. **g**, Western blots showing IRT1 protein levels in *3SS::3xHA-FIT* roots in response to +Fe, +Fe with flg22, -Fe and -Fe with flg22 treatment. HA-tagged FIT protein was blotted using anti-HA antibody. Tubulin protein was blotted as an internal control.

Article

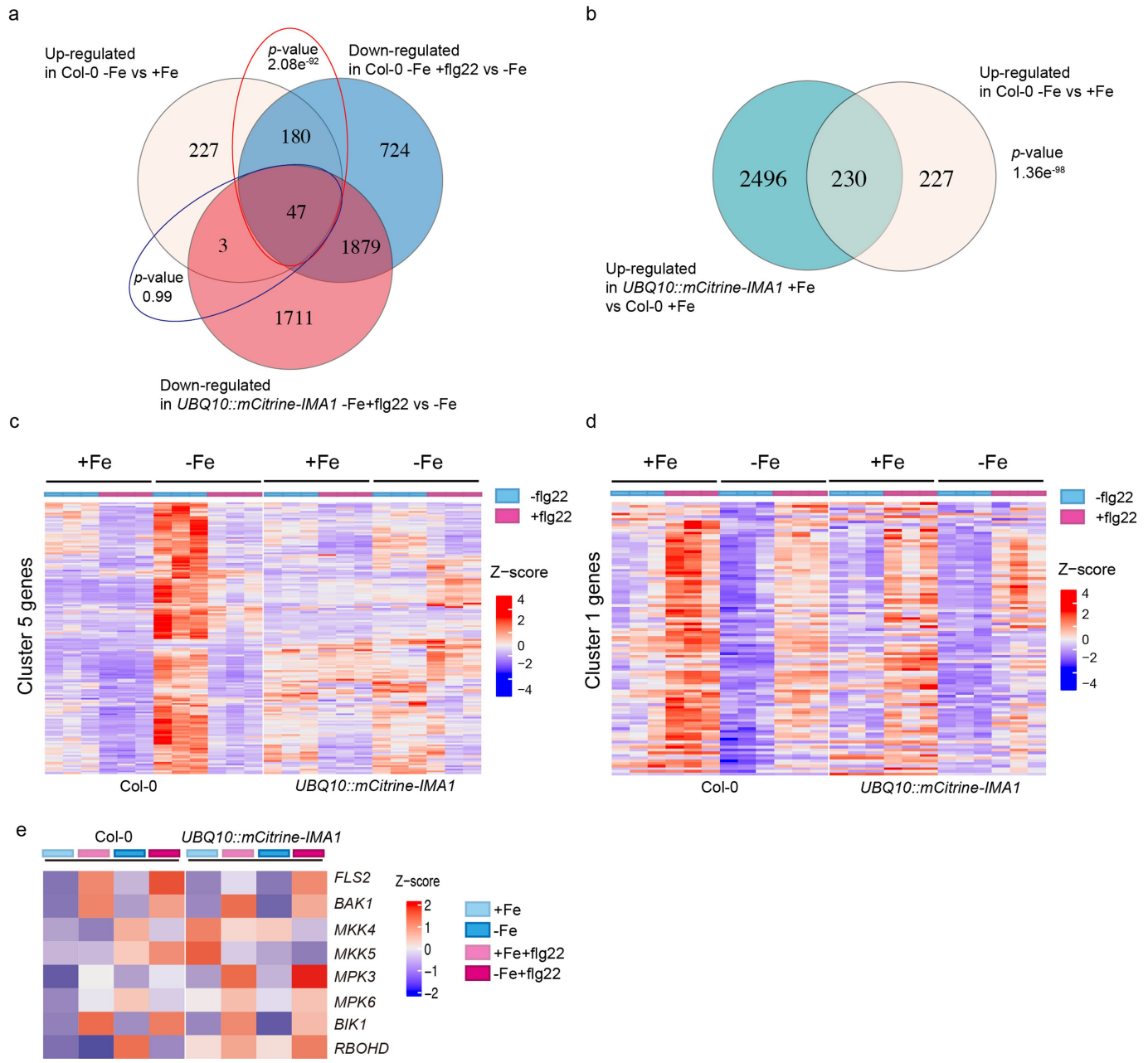


Extended Data Fig. 3 | See next page for caption.

Extended Data Fig. 3 | Flg22 antagonistically regulates the iron deficiency transcriptional landscape through FLS2. **a**, Venn diagram of up/downregulated genes of -Fe versus +Fe, +Fe+flg22 versus +Fe, and -Fe+flg22 versus -Fe, respectively. The statistical analysis of *p*-value was calculated by hypergeometric test (one-sided). **b**, Heat map of mean-centred Z-scores for 1290 differentially expressed genes identified across different treatments (+Fe, +Fe+flg22, -Fe and -Fe+flg22), arranged by *k*-means clustering. Box plot indicates the relative expression level based on median centred Z-score in different clusters. The GO terms analysis was performed using PANTHER17.0 (Fisher's Exact test, *p*-value < 0.05) and indicated on the right side of the heatmap. **c,d**, Heat map of mean-centred Z-scores for differentially

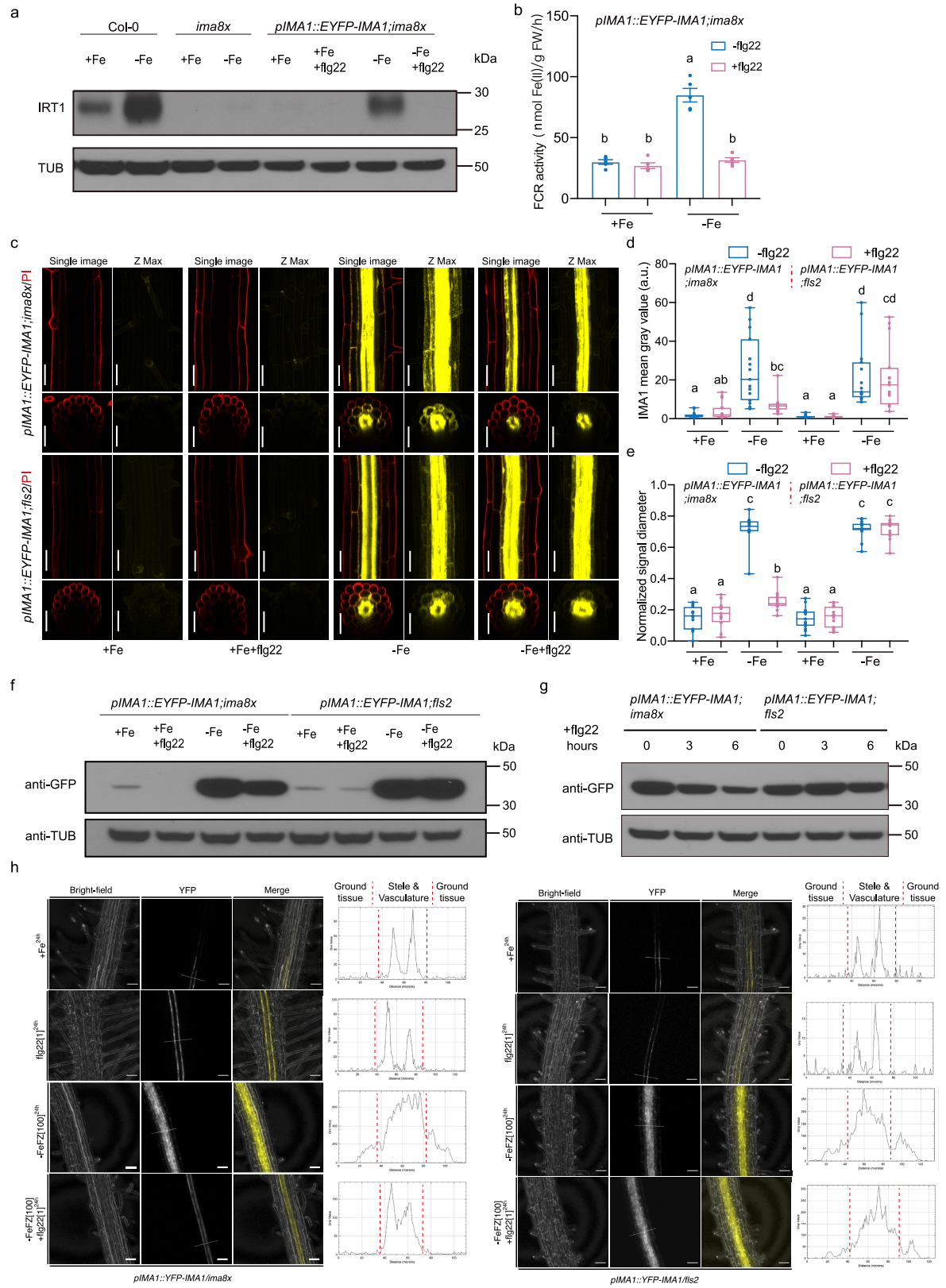
expressed genes (cluster 5 (**c**) and cluster 1 (**d**) in WT and *fls2*) identified across different treatments (+Fe, +Fe+flg22, -Fe and -Fe+flg22), arranged by *k*-means clustering. **e**, Heat map of mean-centred Z-scores (normalized by Col-0 +Fe) for well-known iron responsive genes in response to +Fe, +Fe+flg22, -Fe and -Fe+flg22 in Col-0 and *fls2* roots. **f**, Gene expression analysis in response to +Fe, +Fe with flg22, -Fe and -Fe with flg22 treatment in Col-0 and *fls2* roots by quantitative RT-PCR. The gene expression level is normalized to *ACT2* internal control. The bar chart centres show means of 3 biological replicates. Error bars, s.e.m. Different letters indicate statistically significant differences between different conditions analysed by one-way ANOVA and Tukey's test (*p* < 0.05).

Article



Extended Data Fig. 4 | Flg22 antagonistically regulates the iron deficiency transcriptional landscape through IMA1. **a,b**, Venn diagram of the iron deficiency upregulated genes in Col-0 versus downregulated genes of -Fe+flg22 versus -Fe in Col-0 versus downregulated genes of -Fe+flg22 versus -Fe in *UBQ10::mCitrine-IMA1* (**a**). Venn diagram of the iron deficiency upregulated genes in Col-0 versus upregulated genes in *UBQ10::mCitrine-IMA1* in +Fe versus Col-0 +Fe (**b**). The statistical analysis of p-value was calculated by

hypergeometric test. **c,d**, Heat map of mean-centred Z-scores for differentially expressed genes (cluster 5 and cluster 1 refer to Extended Data Fig. 3b in WT and *UBQ10::mCitrine-IMA1*) identified across different treatments (+Fe, +Fe+flg22, -Fe and -Fe+flg22), arranged by k-means clustering. **e**, Heat map of mean-centred Z-scores (normalized by Col-0 +Fe) for well-known PTI components in response to +Fe, +Fe+flg22, -Fe and -Fe+flg22, respectively.

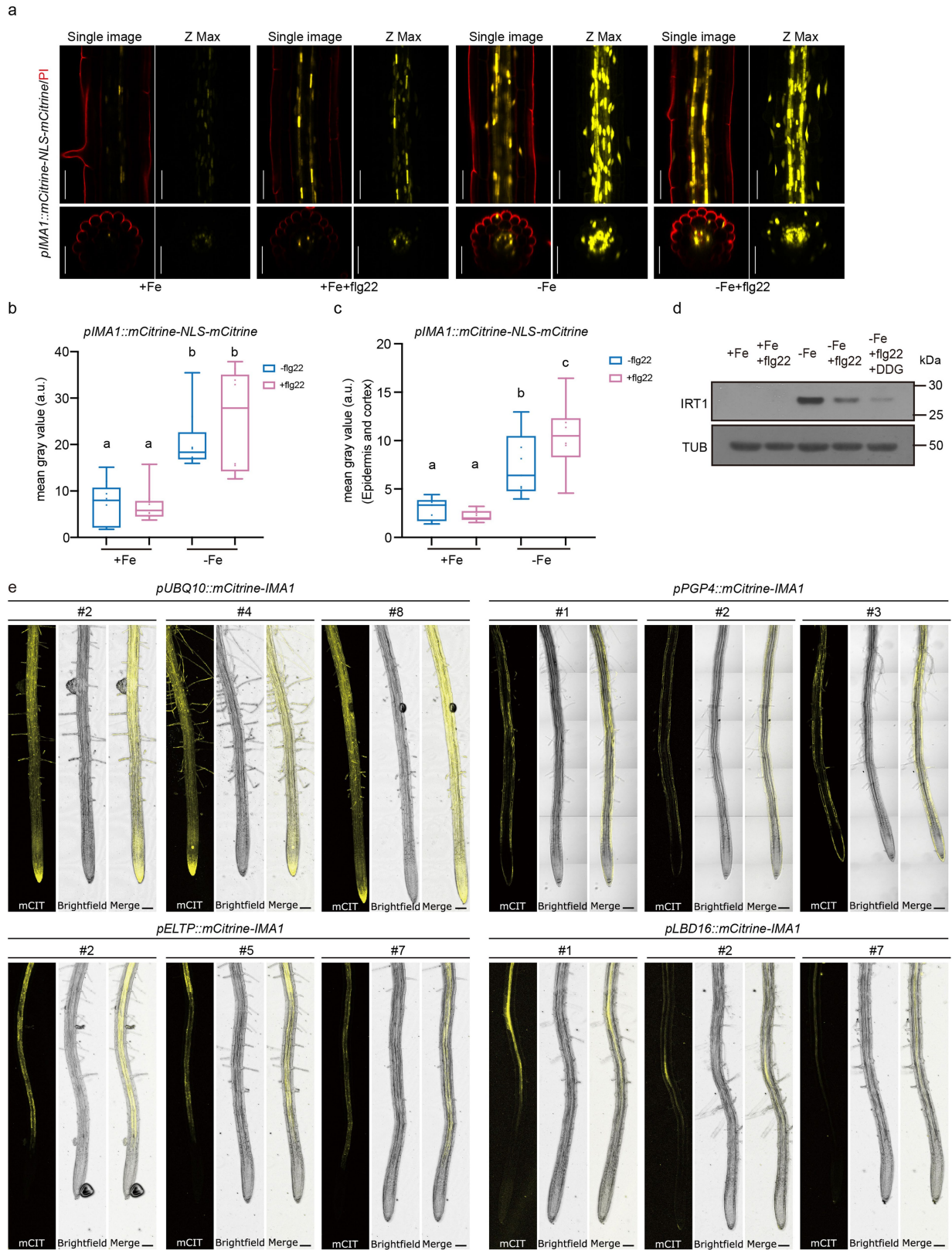


Extended Data Fig. 5 | See next page for caption.

Article

Extended Data Fig. 5 | Flg22 spatially regulates IMA1 protein level in the ground tissue of the root through FLS2. **a**, Western blots showing IRT1 protein levels in Col-0, *ima8x* and *pIMA1::EYFP-IMA1;ima8x* in different treatment conditions. Seedlings were treated with +Fe and -Fe (Col-0 and *ima8x*) and +Fe, +Fe with flg22, -Fe and -Fe with flg22 treatment (*pIMA1::EYFP-IMA1;ima8x*). Tubulin protein was blotted as an internal control. **b**, Quantitative analysis of ferric chelate reductase activities in *pIMA1::EYFP-IMA1;ima8x* roots grown for 7 days under +Fe conditions and transferred to +Fe, +Fe with flg22, -Fe and -Fe with flg22 liquid medium for 2 days. The bar chart centres show mean of 5 biological replicates. Error bars, s.e.m. Different letters indicate statistically significant differences between different conditions analysed by one-way ANOVA and Tukey's test ($p < 0.05$). **c**, IMA1 distribution in response to +Fe, +Fe with flg22, -Fe and -Fe with flg22 treatment in differentiation zone of the root. 5-day-old *pIMA1::EYFP-IMA1;ima8x* and *pIMA1::EYFP-IMA1;fls2* seedlings were grown on the +Fe medium and then transferred to different liquid media for 24 h treatment. The cytosolic and nuclear localized EYFP-IMA1 signals (yellow channel) are visualized with propidium iodide (PI, cell wall staining, red channel). For each treatment, a representative single confocal section (single image, EYFP/PI), a maximal Z-projection of the Z-stack (Z-max, EYFP only), a single optical section of the transverse view, and the Z-projection of the transverse section is shown. Scale bar, 50 μ m. **d,e**, Quantification of IMA1 fluorescence

signal intensity (**d**) and normalized IMA1 signal diameter (**e**) in response to +Fe, +Fe with flg22, -Fe and -Fe with flg22 treatment in differentiation zone of the root in *pIMA1::EYFP-IMA1;ima8x* and *pIMA1::EYFP-IMA1;fls2* ($n = 15$ biologically independent seedlings from 3 biological repeats). The same dataset from Fig. 3d,f of *pIMA1::EYFP-IMA1;ima8x* were used here as the images for quantification were taken at the same time. Different letters indicate statistically significant differences between different conditions analysed by Kruskal Wallis/two tailed test followed by Multiple pairwise comparisons using the Steel-Dwass-Critchlow-Fligner procedure/two-tailed test ($p < 0.05$). **f**, Western blots showing IMA1 protein levels in the roots of *pIMA1::EYFP-IMA1;ima8x* and *pIMA1::EYFP-IMA1;fls2* in +Fe, +Fe with flg22, -Fe and -Fe with flg22 treatments. Tubulin protein was blotted as an internal control. **g**, Western blots showing IMA1 protein levels in *pIMA1::EYFP-IMA1;ima8x* and *pIMA1::EYFP-IMA1;fls2* roots. The seedlings were pre-treated with -Fe for 36 h, then treated with -Fe+flg22 (1 μ m flg22) for 0, 3 and 6 h. Tubulin protein was blotted as an internal control. **h**, Representative image of EYFP-IMA1 signal intensity profile in response to +Fe, +Fe with flg22, -Fe and -Fe with flg22 treatment in differentiation zone of root in *pIMA1::EYFP-IMA1;ima8x* (left panel) and *pIMA1::EYFP-IMA1;fls2* (right panel). The white line in YFP channel indicates the line for signal quantification. The red dashed lines indicate the boundary between the ground tissue and the stele. Scale bar, 50 μ m.

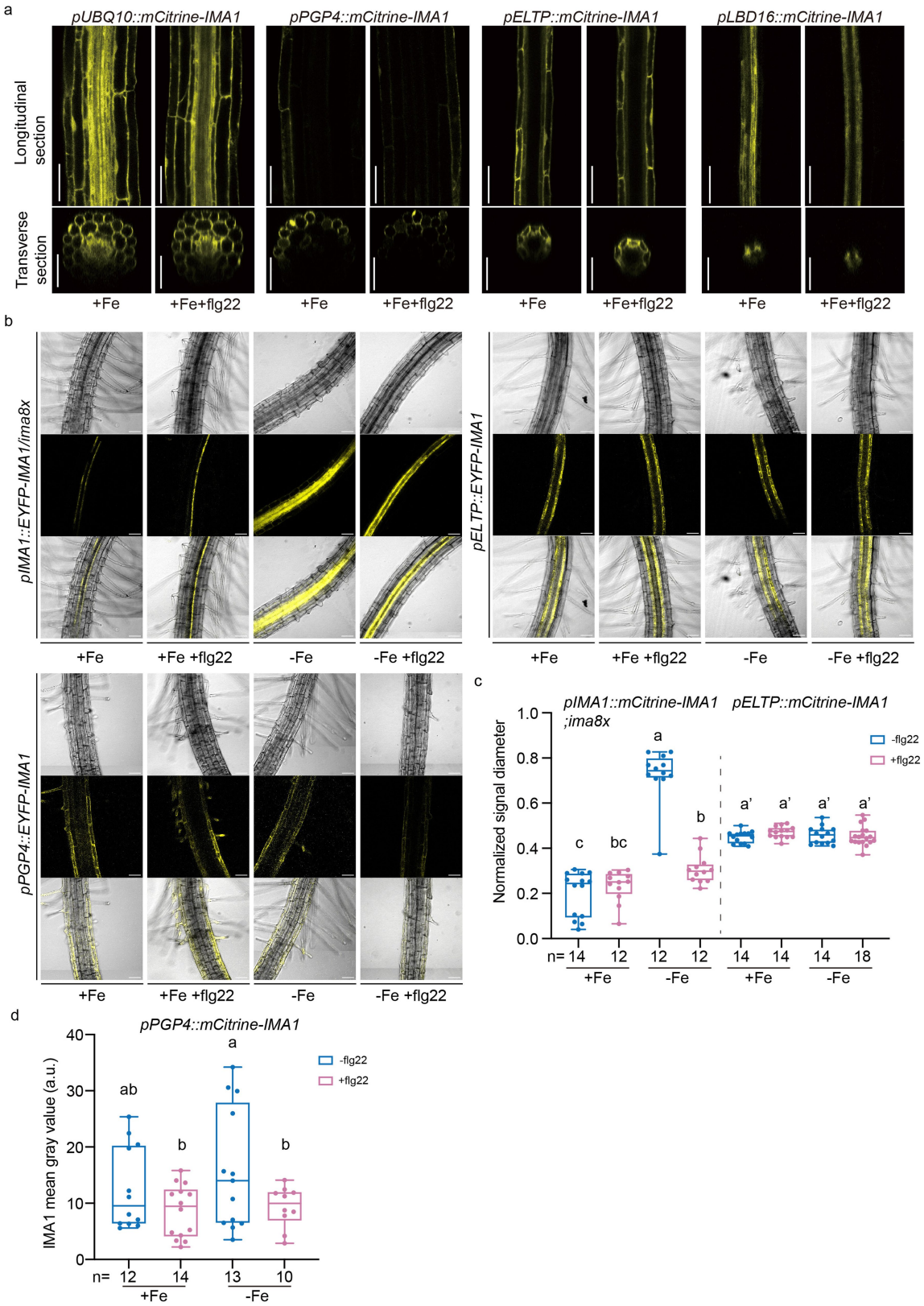


Extended Data Fig. 6 | See next page for caption.

Article

Extended Data Fig. 6 | Flg22 does not fully repress *IMA1* transcription in the ground tissue and flg22 dependent callose deposition is not required for IRT1 repression. **a**, Promoter activity of *IMA1* in the root of *pIMA1::mCitrine-NLS-mCitrine* seedlings in response to +Fe, +Fe with flg22, -Fe and -Fe with flg22 treatment. 5-day-old seedlings were grown on the +Fe medium and then transferred to the different liquid media for 24 h treatment. The nuclear localized mCitrine signals (Yellow channel) are visualized with propidium iodide (PI, red channel). For each treatment, a representative single confocal section (single image, GFP/PI), maximum intensity Z-projection (Z-max, GFP only), a single optical section of the transverse view, and the Z-projection of the

transverse section is shown. Scale bar, 50 μ m. **b,c**, Normalized *IMA1* promoter activity quantification in all cell layers (**b**) or in epidermis-cortex cell layers (**c**) in response to +Fe, +Fe+flg22, -Fe and -Fe+flg22 treatments ($n = 9, 3$ repeats). Different letters indicate statistically significant differences between different conditions analysed by one-way ANOVA and Fisher's LSD test(two-sided, $p < 0.05$). **d**, Western blots showing IRT1 protein levels in Col-0 roots is in response to +Fe, +Fe with flg22, -Fe, -Fe with flg22 treatment and -Fe with flg22 and DDG treatment. Tubulin protein was blotted as an internal control. **e**, Representative images of cell-layer specific *IMA1* expression transgenic plants. 3 individual lines are shown under +Fe condition. Scale bar, 100 μ m.

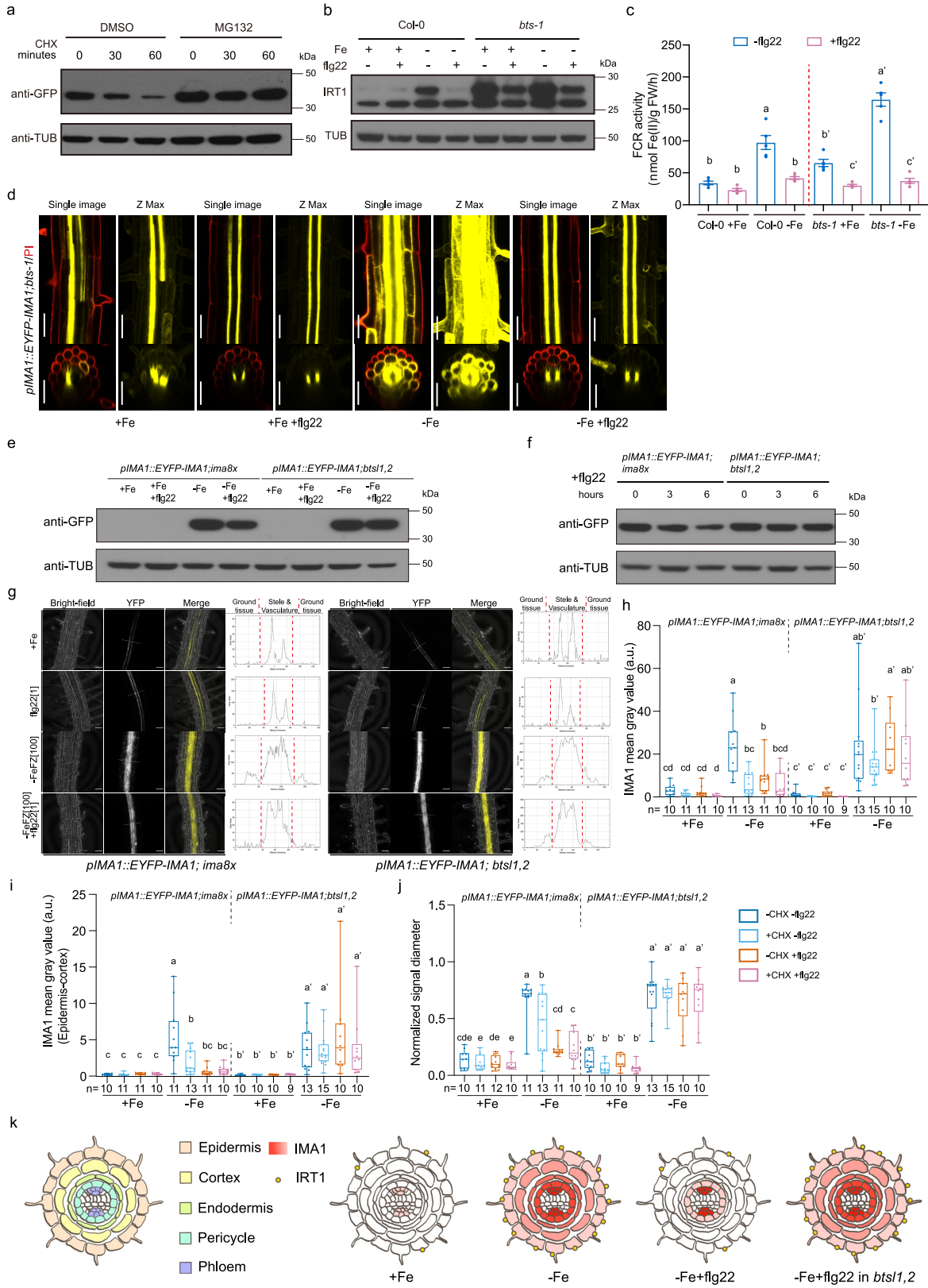


Extended Data Fig. 7 | See next page for caption.

Article

Extended Data Fig. 7 | IMA1 is not regulated through cell-to-cell movement but regulated through protein level in the epidermis-cortex under -Fe by flg22. **a**, Representative images of roots of plants with different tissue-specific promoters driving IMA1 expression. 5-day-old transgenic seedlings were grown on +Fe solid medium and then transferred to +Fe or +Fe+flg22 liquid medium for 24 h treatment. For each treatment, the cytosolic and nuclear-localized mCitrine-IMA1 signals (yellow channel) are visualized with longitudinal section and transverse section. Scale bar, 50 μ m. **b**, Representative images of roots of plants with *pIMA1*, *pELTP* or *pPGP4* promoters driving IMA1 expression in response to +Fe, +Fe+flg22, -Fe and -Fe+flg22. For each treatment,

mCitrine-IMA1 signals (yellow channel) and bright field are visualized with longitudinal section. Scale bar, 50 μ m. **c**, Quantification of normalized IMA1 signal diameter in different treatment conditions in differentiation zones of the roots. Different letters indicate statistically significant differences between different conditions analysed by one-way ANOVA and Fisher's LSD test (two-sided, $p < 0.05$). **d**, Quantification of normalized IMA1 signal intensity of *pPGP4::mCitrine-IMA1* in different treatment conditions. Different letters indicate statistically significant differences between different conditions analysed by one-way ANOVA and Fisher's LSD test (two-sided, $p < 0.05$).

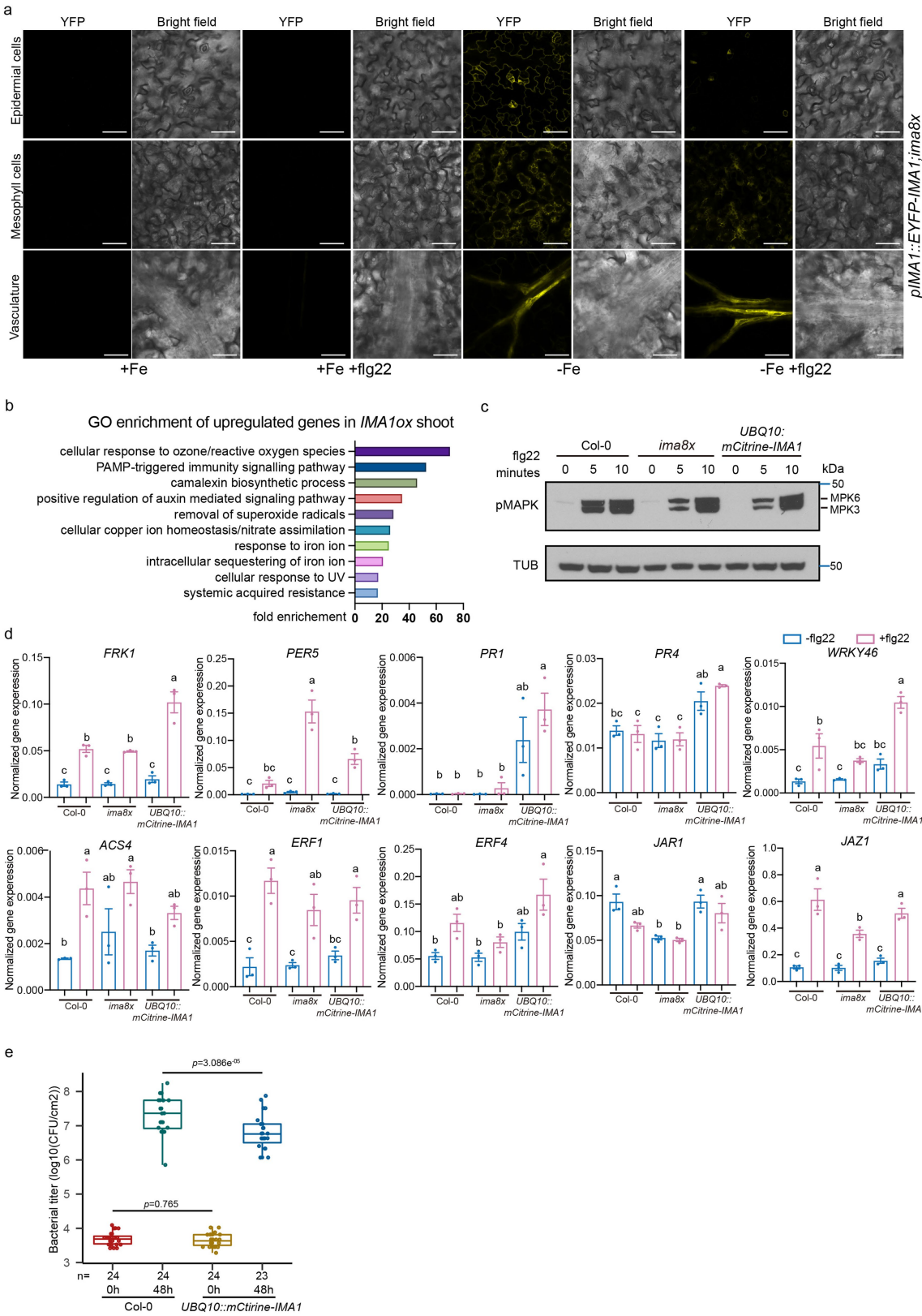


Extended Data Fig. 8 | See next page for caption.

Article

Extended Data Fig. 8 | Flg22 dependent IMA1 degradation in the ground tissue is regulated by BTSL1 and BTSL2 but not by BTS. **a**, Western blots showing IMA1 protein is degraded through ubiquitin-dependent proteasome mechanism under -Fe condition. The *p/IMA1::EYFP-IMA1;ima8x* was pre-treated with -Fe with DMSO only or -Fe with 10 μ M MG132 for 36 h, subsequently with 100 μ M Cycloheximide (CHX) for the indicated time period. Tubulin protein was blotted as an internal control. **b**, Western blots showing IRT1 protein levels in Col-0 and *bts-1* roots in +Fe, +Fe with flg22, -Fe and -Fe with flg22 treatment. Tubulin protein was blotted as an internal control. **c**, Quantitative analysis of Ferric Chelate Reductase activities in Col-0 and *bts-1* roots grown for 7 days under +Fe conditions and transferred to +Fe, +Fe with flg22, -Fe and -Fe with flg22 liquid medium for 2 days. The bar chart centres show mean of 5 biological replicates. Error bars, s.e.m. Different letters indicate statistically significant differences between different conditions analysed by one-way ANOVA and Tukey's test ($p < 0.05$). **d**, IMA1 distribution in *bts-1* in response to +Fe, +Fe with flg22, -Fe and -Fe with flg22 treatment in differentiation zone of the root. 5-day-old *p/IMA1::EYFP-IMA1;bts-1* seedlings were grown on the +Fe medium and then transferred to different liquid medium for 24 h treatment. The cytosolic and nuclear localized EYFP-IMA1 signals (yellow channel) are visualized with propidium iodide (PI, red channel). For each treatment, a representative single confocal section (single image, EYFP/PI), a maximal Z-projection of the Z-stack (Z-max, EYFP only), a single optical section of the transverse view, and the Z-projection of the transverse section is shown. Scale bar, 50 μ m. **e**, Western

blots showing IMA1 protein levels in the roots of *p/IMA1::EYFP-IMA1;ima8x* and *p/IMA1::EYFP-IMA1;bts1,2* in +Fe, +Fe with flg22, -Fe and -Fe with flg22 treatments. Tubulin protein was blotted as an internal control. **f**, Western blots showing IMA1 protein levels in *p/IMA1::EYFP-IMA1;ima8x* and *p/IMA1::EYFP-IMA1;bts1,2* roots. The seedlings were pretreated with -Fe for 36 h, then treated with -Fe+flg22 (1 μ M flg22) for 0, 3 and 6 h. Tubulin protein was blotted as an internal control. **g**, Representative image of EYFP-IMA1 signal intensity profile in response to +Fe, +Fe with flg22, -Fe and -Fe with flg22 treatment in differentiation zone of roots in *p/IMA1::EYFP-IMA1;ima8x* and *p/IMA1::EYFP-IMA1;bts1,2*. The white line in YFP channel indicates the line for signal quantification. The red dashed lines indicate the boundary between the ground tissue and the stele. Scale bar, 50 μ m. **h-j**, Quantification of normalized total IMA1 signal intensity (**h**), normalized IMA1 signal intensity in epidermis and cortex (**i**) and IMA1 signal diameter (**j**) in differentiation zone of roots in *p/IMA1::EYFP-IMA1;ima8x* and *p/IMA1::EYFP-IMA1;bts1,2*. The seedlings were pretreated with +Fe/-Fe 36 h with/without flg22 and treated with 100 μ M CHX for 2 h before imaging. Different letters indicate statistically significant differences between different conditions analysed by one-way ANOVA and Fisher's LSD test (two-sided, $p < 0.05$). **k**, Schematic of flg22-mediated IMA1 depletion in the outer cell layers (epidermis, cortex, and endodermis) and IRT1 repression in epidermis in response to +Fe, -Fe and -Fe with flg22 treatment respectively. By contrast, IMA1 is not fully degraded in *bts1,2* in the outer cell layers upon flg22 treatment, resulting in IRT1 level maintenance in epidermis.

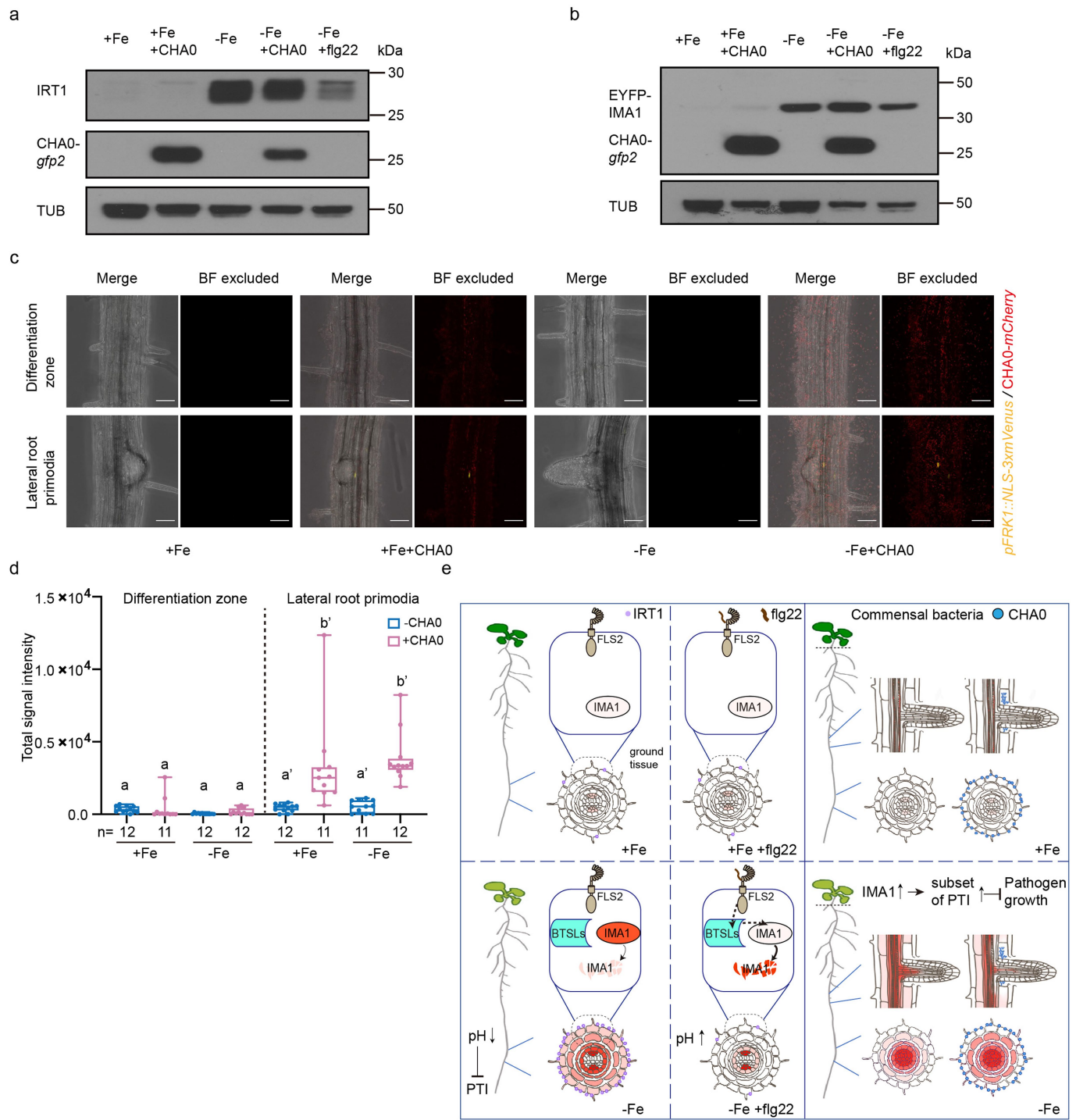


Extended Data Fig. 9 | See next page for caption.

Article

Extended Data Fig. 9 | IMA1 mediates defence responses to different pathogens in the shoot. **a**, Confocal images of *pIMAI::EYFP-IMAI;ima8x* responses to +Fe, +Fe with flg22, -Fe and -Fe with flg22 in the shoot. Three different zones were imaged: epidermal cells, mesophyll cells and vasculature. The cytosolic and nuclear localized EYFP-IMAI signals (yellow channel) are visualized with bright field (bright field channel). For each treatment, a representative single confocal section is shown. Scale bar, 50 μ m. **b**, Gene ontology analysis of upregulated genes in *IMAIox* compared with Col-0 in the shoot. GO term analysis is performed by using PANTHER17.0 (p -value < 0.05). X axis, fold enrichment. **c**, Western blots showing MAPK phosphorylation by flg22 in Col-0, *ima8x* and *UBQ10::mCitrine-IMAI* shoot in response to flg22. The shoot parts were treated with 1 μ M flg22 for 0, 5 and 10 min. Tubulin protein was blotted as an internal control. **d**, Gene expression analysis in response to +Fe and +Fe with flg22 by quantitative RT-PCR. The gene

expression level is normalized to *ACT2* internal control. The shoot parts were treated with 1 μ M flg22 for 1 h. The bar chart centres show means of 3 biological replicates and error bars show s.e.m. Different letters indicate statistically significant differences between different conditions analysed by one-way ANOVA and Tukey's test (p < 0.05). **e**, Growth of *Pseudomonas syringae* pv. *tomato* DC3000 in the leaves of Col-0 and *UBQ10::mCitrine-IMAI*. Bacteria were syringe-infiltrated at OD_{600} = 0.001, and bacterial colony forming units (CFUs) were counted 0 and 48 h after inoculation (hpi). n = 22–24 biological replicates from three independent experiments. Different letters indicate statistically significant differences (adjusted P < 0.01; two-tailed Student's t-test followed by Benjamini–Hochberg method). Results are shown as box plots with boxes displaying the 25th–75th percentiles, the centre line indicating the median and whiskers extending to the minimum and maximum values no further than 1.5 \times interquartile range.



Extended Data Fig. 10 | See next page for caption.

Article

Extended Data Fig. 10 | IRT1 and IMA1 accumulation is distinctly regulated by CHAO or flg22 peptide. **a**, Western blots showing IRT1 protein levels in Col-0 roots in response to +Fe, +Fe+CHAO, -Fe, -Fe+CHAO and -Fe+flg22 treatments. The inoculation of CHAO-gfp2 was detected by anti-GFP western blot. Tubulin protein was blotted as an internal control. **b**, Western blots showing IMA1 protein levels in *pIMA1::EYFP-IMA1;ima8x* roots in response to +Fe, +Fe+CHAO, -Fe, -Fe+CHAO and -Fe+flg22 treatment. The EYFP-IMA1 and the inoculation of CHAO-gfp2 were detected by anti-GFP western blot. Tubulin protein was blotted as an internal control. **c**, The promoter activity of *FRK1* in *pFRK1::NLS-3xmVenus* roots in responses to +Fe, +Fe+CHAO, -Fe, -Fe+CHAO in differentiation zone or at lateral root primordia. Scale bar, 50 μ m. **d**, Quantification of the total signal intensity of the promoter activity of *FRK1* in response to +Fe, +Fe+CHAO, -Fe, -Fe+CHAO in differentiation zone or at lateral root primordia. Different letters indicate statistically significant differences between different conditions analysed by one-way ANOVA and Fisher's LSD test ($p < 0.05$). **e**, Graphical summary of main findings. Red colour gradient indicates IMA1 abundance. Left and middle columns: IMA1 and IRT expression in the root under +Fe (upper left), -Fe (lower left), +Fe + flg22

(upper middle), -Fe + flg22 (lower middle). In +Fe IMA1 and IRT1 are expressed at very low levels in the early differentiation zone of the root. In -Fe, IMA1 highly accumulates in the ground tissue of the root under; roots actively lower the rhizosphere pH and increase iron availability, but this decreases PTI responsiveness. In -Fe and flg22 treatment, IMA1 is degraded in a BTSL dependent manner. The rhizosphere pH is not decreased. Right column: IMA1 accumulation in relation to root and shoot host-microbe interactions. Upper right: In +Fe conditions IMA1 levels are low and don't respond to commensal bacteria CHAO. Lower right: high levels IMA1 enhances a subset of PTI in the shoot. In -Fe IMA1 is accumulated in the root. In the early differentiation zone, surface dwelling CHAO bacteria don't affect IMA1 levels; high IMA1 levels increase bacterial colonization on the surface. When CHAO colonizes inner root tissues at lateral root primordia cracks, IMA1 decreases in cells adjacent to this colonization. IMA1 accumulation is distinctly regulated by CHAO in early differentiation zone compared to emerging LR region. The differences in IMA1 signal intensity between the depictions in the panels relating to CHAO are due to different experiment settings (half sucrose concentration and different laser power for real bacteria experiment; see methods section).

Reporting Summary

Nature Portfolio wishes to improve the reproducibility of the work that we publish. This form provides structure for consistency and transparency in reporting. For further information on Nature Portfolio policies, see our [Editorial Policies](#) and the [Editorial Policy Checklist](#).

Statistics

For all statistical analyses, confirm that the following items are present in the figure legend, table legend, main text, or Methods section.

n/a Confirmed

- The exact sample size (n) for each experimental group/condition, given as a discrete number and unit of measurement
- A statement on whether measurements were taken from distinct samples or whether the same sample was measured repeatedly
- The statistical test(s) used AND whether they are one- or two-sided
Only common tests should be described solely by name; describe more complex techniques in the Methods section.
- A description of all covariates tested
- A description of any assumptions or corrections, such as tests of normality and adjustment for multiple comparisons
- A full description of the statistical parameters including central tendency (e.g. means) or other basic estimates (e.g. regression coefficient) AND variation (e.g. standard deviation) or associated estimates of uncertainty (e.g. confidence intervals)
- For null hypothesis testing, the test statistic (e.g. F , t , r) with confidence intervals, effect sizes, degrees of freedom and P value noted
Give P values as exact values whenever suitable.
- For Bayesian analysis, information on the choice of priors and Markov chain Monte Carlo settings
- For hierarchical and complex designs, identification of the appropriate level for tests and full reporting of outcomes
- Estimates of effect sizes (e.g. Cohen's d , Pearson's r), indicating how they were calculated

Our web collection on [statistics for biologists](#) contains articles on many of the points above.

Software and code

Policy information about [availability of computer code](#)

Data collection All the confocal images are acquired from Zen Microscopy software (ZEISS).
The RNAseq data was collected through the Illumina Nextseq2000 platform

Data analysis All the data analysis of confocal images are done using Fiji (Image J) (Version 2.1.0)
The RNAseq analysis was performed by R software (Version 4.0.2)
The statistical analysis was performed by GraphPad Prism 9 and XLSTAT 2020.4.1.1032
The code for imaging quantification and RNAseq analysis are available at <https://github.com/cm010713/immunity-iron-project>
Gene ontology enrichment analysis was conducted using online tools of GENEONTOLOGY website: <http://geneontology.org/>

For manuscripts utilizing custom algorithms or software that are central to the research but not yet described in published literature, software must be made available to editors and reviewers. We strongly encourage code deposition in a community repository (e.g. GitHub). See the Nature Portfolio [guidelines for submitting code & software](#) for further information.

Data

Policy information about [availability of data](#)

All manuscripts must include a [data availability statement](#). This statement should provide the following information, where applicable:

- Accession codes, unique identifiers, or web links for publicly available datasets
- A description of any restrictions on data availability
- For clinical datasets or third party data, please ensure that the statement adheres to our [policy](#)

Raw sequencing data of RNAseq have been uploaded to NCBI GEO database: GSE213557. Uncropped gel and blot source data are provided in Supplementary Figure 1. Source data (with statistical analysis) are provided with this paper in the supplementary files. Gene sequence for RNAseq reads mapping were obtained from TAIR10 reference genome.

Human research participants

Policy information about [studies involving human research participants and Sex and Gender in Research](#).

Reporting on sex and gender

N/A

Population characteristics

N/A

Recruitment

N/A

Ethics oversight

N/A

Note that full information on the approval of the study protocol must also be provided in the manuscript.

Field-specific reporting

Please select the one below that is the best fit for your research. If you are not sure, read the appropriate sections before making your selection.

Life sciences Behavioural & social sciences Ecological, evolutionary & environmental sciences

For a reference copy of the document with all sections, see nature.com/documents/nr-reporting-summary-flat.pdf

Life sciences study design

All studies must disclose on these points even when the disclosure is negative.

Sample size

Sample size are described in the relevant figure legends or in the figure panels. Sample size determination is based on experimental trials and with consideration of previous publications (eg. chlorophyll concentration measurement:DOI:10.1093/jxb/ert153; iron concentration measurement: <https://doi.org/10.1016/j.molp.2018.06.005>; FCR activity: <https://doi.org/10.1038/s41477-018-0266-y>; Imaging and root growth:<https://doi.org/10.1016/j.cell.2020.01.013> and <https://doi.org/10.1038/s41467-022-32167-6>) Cf u counts assay: <https://doi.org/10.1016/j.cell.2020.01.013>.) There were no statistical methods used to predetermine sample size.

Data exclusions

No data that pass quality control were excluded from statistical analysis.

Replication

The experiments are repeated at least 3 times with consistent results except for the western blot of Figure 3G were repeated for two times and showing consistent results.

Randomization

Plants were grown side-by-side randomly in the growth chamber. The seedlings were randomly picked from the plate for treatment or relevant experiment. For liquid treatment, seedlings were distributed randomly in each well of six well plates.

Blinding

Investigators were not blinded to the allocation in the experiments which do not contain clinical trials. The research materials need to be strictly regulated and clearly labeled as they were gene edited plants. This also because plants with different treatments can exhibit phenotypes that make them visually identifiable. The phenotype was observed/assessed by more than one author. The imaging experiments are performed by double blind. (Different person in our lab or in the collaborator's lab)

Reporting for specific materials, systems and methods

We require information from authors about some types of materials, experimental systems and methods used in many studies. Here, indicate whether each material, system or method listed is relevant to your study. If you are not sure if a list item applies to your research, read the appropriate section before selecting a response.

Materials & experimental systems

n/a	Involved in the study
<input type="checkbox"/>	<input checked="" type="checkbox"/> Antibodies
<input checked="" type="checkbox"/>	<input type="checkbox"/> Eukaryotic cell lines
<input checked="" type="checkbox"/>	<input type="checkbox"/> Palaeontology and archaeology
<input checked="" type="checkbox"/>	<input type="checkbox"/> Animals and other organisms
<input checked="" type="checkbox"/>	<input type="checkbox"/> Clinical data
<input checked="" type="checkbox"/>	<input type="checkbox"/> Dual use research of concern

Methods

n/a	Involved in the study
<input checked="" type="checkbox"/>	<input type="checkbox"/> ChIP-seq
<input checked="" type="checkbox"/>	<input type="checkbox"/> Flow cytometry
<input checked="" type="checkbox"/>	<input type="checkbox"/> MRI-based neuroimaging

Antibodies

Antibodies used

Anti-IRT1 primary antibody (Agrisera Cat. AS111780)
 Goat Anti-Rabbit IgG (H+L)-HRP Conjugate (Bio-Rad Cat.170-6515)
 Anti-MPK p44/42 (Cell Signaling Cat. 4370)
 Anti-GFP HRP conjugate (Miltenyi Biotec Cat. 130-091-833)
 Anti-HA HRP conjugate (Roche Cat. 12013819001)
 Anti-Tubulin (Invitrogen Cat. 32-2500)
 Goat Anti-Mouse IgG (H+L)-HRP Conjugate (Bio-Rad Cat. 170-6516)

Validation

The Anti-IRT1 primary antibody is validated in this study using irt1-1 mutant in arabidopsis thaliana through western blot (extended data figure 1f in this study). The official application examples is provided by Agrisera: <https://www.agrisera.com/en/artiklar/irt1-iron-regulated-transporter-1.html>.
 The Anti-MPK 44/42 antibody was validated by published literature (Ngou, B.P.M., Ahn, HK., Ding, P. et al. Mutual potentiation of plant immunity by cell-surface and intracellular receptors. *Nature* 592, 110–115 (2021).) Official supporting information: <https://www.cellsignal.com/products/primary-antibodies/phospho-p44-42-mapk-erk1-2-thr202-tyr204-d13-14-e-xp-rabbit-mab/4370>
 The Anti-GFP HRP conjugate antibody was validated by published literature (Jaillais Y, Hothorn M, Belkhadir Y, Dabi T, Nimchuk ZL, Meyerowitz EM, Chory J. Tyrosine phosphorylation controls brassinosteroid receptor activation by triggering membrane release of its kinase inhibitor. *Genes Dev.* 2011 Feb 1;25(3):232-7.) Official supporting information: <https://www.miltenyibiotec.com/US-en/products/gfp-antibody-gg4-2c2-12-10.html>
 Anti-HA HRP conjugate: <https://www.sigmaaldrich.com/US/en/product/roche/12013819001>
 Anti-Tubulin: <https://www.thermofisher.com/antibody/product/alpha-Tubulin-Antibody-clone-B-5-1-2-Monoclonal/32-2500>
 The secondary antibodies (Goat Anti-Rabbit IgG (H+L)-HRP Conjugate (Bio-Rad Cat.170-6515) & Goat Anti-Mouse IgG (H+L)-HRP Conjugate (Bio-Rad Cat. 170-6516)) were validated by published literature (Cao, M., Chen, R., Li, P. et al. TMK1-mediated auxin signalling regulates differential growth of the apical hook. *Nature* 568, 240–243 (2019). <https://doi.org/10.1038/s41586-019-1069-7>) Official supporting information: Goat Anti-Rabbit IgG (H+L)-HRP Conjugate: <https://www.bio-rad.com/en-us/sku/1706515-goat-anti-rabbit-igg-h-l-hrp-conjugate?ID=1706515> ; Goat Anti-Mouse IgG (H+L)-HRP Conjugate: <https://www.bio-rad.com/en-us/sku/1706516-goat-anti-mouse-igg-h-l-hrp-conjugate?ID=1706516>